

Suppression of decoherence dynamics by a dissipative bath at strong coupling

Jitian Chen^{x, 1,*}, Jakub Garwoła^{x, 2, †} and Dvira Segal^{1, 2, ‡}

¹*Department of Chemistry, University of Toronto, 80 Saint George St., Toronto, Ontario, M5S 3H6, Canada*

²*Department of Physics and Centre for Quantum Information and Quantum Control,
University of Toronto, 60 Saint George St., Toronto, Ontario, M5S 1A7, Canada*

(Dated: April 4, 2025)

Control of decoherence in open quantum systems has become a topic of great interest due to the emergence of quantum technologies that depend on quantum coherent effects. In this work, we investigate the decoherence dynamics of systems coupled to multiple baths through noncommuting systems' operators, and beyond the weak system-bath coupling limit. By building on cooperative effects between baths, we propose a novel strategy to mitigate rapid decoherence. Concretely, we study the dynamics of a qubit coupled to multiple environments with arbitrary interaction strengths, and along different coordinates. Based on insights gained on the decoherence dynamics from the analytical Effective Hamiltonian method, we carry out numerical simulations using the Reaction Coordinate quantum master equation method. In contrast to standard expectations, we show that when the system strongly interacts with a decohering bath, increasing its coupling to a second, dissipative bath *slows down* the decoherence dynamics. Our work offers insights into the preservation of quantum coherences in open quantum systems based on frustration effects, by utilizing cooperative effects between different heat baths.

I. INTRODUCTION

Quantum coherence is an important property of quantum mechanical systems, which describes the “quantumness” of the system, or the ability for quantum states to interfere, and the system to exhibit nonclassical behaviors such as quantum entanglement [1, 2]. Quantum coherences enable for a wide range of applications [1, 2]: In quantum computing, it is essential to maintain superpositions and entanglement for quantum speedup in algorithms [3]. In quantum metrology, quantum coherences can enhance measurement precision beyond the classical limit [4]. Quantum communication protocols leverage coherence to achieve secure information transfer [5]. Moreover, coherences between quantum states play a fundamental role in other areas, such as coherent control of chemical reactions [6] and charge and energy transfer on the molecular scale [7].

Noisy Intermediate-Scale Quantum (NISQ) devices represent the current generation of quantum processors, characterized by a limited number of qubits and the absence of error correction [8, 9]. Due to unavoidable crosstalk and interactions with their environments, these devices experience decoherence and relaxation, which degrade their quantum state over time. Two phenomenological parameters quantify these errors: the population relaxation time, T_1 , and the phase decoherence time, T_2 . The relaxation (or dissipation) time T_1 describes the timescale over which a qubit loses energy due to dissipative processes. The decoherence time T_2 quantifies the loss of phase coherence in a superposition state, arising from both the energy relaxation and the pure dephasing mechanisms. These timescales eventually determine the fidelity

of quantum computations and the feasibility of running deep quantum circuits on NISQ hardware [10]. Extending these times is therefore a central challenge in the development of quantum processing units.

Dynamical decoupling (DD) is a prominent strategy in fighting against decoherence. It involves a sequence of pulses designed to counteract the effect of the environment and essentially decouple the system from it [11–17]. Other methods include the Quantum Zeno Effect (QZE), Quantum Error Correction (QEC), and Optimal Control Theory (OCT) [18, 19]. QZE relies on frequent measurements to inhibit the evolution of a quantum system, QEC detects and corrects errors through redundancy and feedback mechanisms, and OCT employs numerical optimization to design time-dependent pulse sequences that minimize decoherence. All of these involve time-varying operations to counteract decoherence [20–22]. Unlike these and other time-dependent control schemes [18, 19, 23], the approach described in this work is autonomous; it does not involve time-dependent fields.

A wealth of theoretical approaches have been developed to describe the effect of energy dissipation and quantum decoherence in open quantum systems [24, 25]. In this work, we use the quantum master equation (QME) family of method. The well-known Redfield QME is derived from microscopic principles under the assumption of Markovian dynamics and weak couplings to the baths [25], leading to additive impacts of the baths on the system. However, these limitations can be overcome using Markovian embedding methods: In essence, Markovian embedding works by redefining the system-bath boundary, allowing a Markovian weak-coupling approach to be applied to an extended system.

Since its inception for studying chemical reactions [26, 27], the Reaction Coordinate (RC) method—a Markovian embedding technique—has gained increasing attention as a powerful and easy-to-implement approach for open quantum systems [28]. Essentially, this method involves performing simulations using Lindblad or Redfield QMEs within an extended Hilbert space, where the system remains weakly coupled to

^x These authors contributed equally to this work.

* jitian.chen@mail.utoronto.ca

† jakub.garwola@mail.utoronto.ca

‡ dvira.segal@utoronto.ca

a residual environment assumed to be Markovian. We refer to this computational framework as RC-QME simulation. Recently, RC-QME simulations have been applied to various problems, including pure decoherence dynamics [29], quantum dissipation in impurities [30] and their steady state [31], quantum thermal transport [32–38], dissipation-engineered magnetic order [39], as well as fermionic transport [40–43]. However, while powerful, the RC-QME method primarily yields numerical results rather than analytical insights, and thus does not provide a clear strategy to suppress or eliminate decoherence and relaxation processes.

Complementing numerical techniques such as the RC-QME, a promising analytical approach, the Effective Hamiltonian (EFFH) method, has recently been developed in Ref. 44. The EFFH method begins by extracting a collective reaction coordinate mode from each harmonic bath, similar to the RC mapping. Then, a polaron transformation is applied, followed by a truncation of the polaron-shifted reaction coordinate modes, thus yielding the so-called Effective Hamiltonian. In this framework, strong coupling effects are encoded in renormalized parameters, those of the system, and of its interaction with the baths. The EFFH method has been proven to be valuable for studying the dynamics [45], equilibrium properties [46, 47], and nonequilibrium steady states [44] of various open quantum system models with arbitrary coupling strengths. Recently, the EFFH framework was further extended to handle systems coupled to multiple baths through noncommuting system's operators [45].

To explore the interplay between decoherence and relaxation, we consider the setup illustrated in Fig. 1, where a qubit is coupled to multiple heat baths through noncommuting system operators. The suppression of population relaxation by enhancing the coupling of a qubit to a decohering (z) bath was demonstrated numerically in Ref. [48, 49]. It was later analytically explained in Ref. 45. However, in a previous study the decoherence rate was shown to always increase with increasing any of the couplings to the two baths [49]. In contrast, in this work, we uncover the highly nonintuitive effect of *suppressing decoherence by increasing* the coupling of the system to a dissipative bath. This effect arises from cooperative effects between the baths, leading to “frustration”, which is induced by the noncommutativity of system operators beyond the weak coupling limit. Combining numerical and analytical techniques, we predict the existence of this effect, identify the parameter regimes in which it manifests, and demonstrate it with simulations.

Our main findings are twofold. First, we derive the effective Hamiltonian for the model in Fig. 1, given in Eq. (16). Beyond its relevance to study quantum impurity dynamics and their steady-state properties, this effective Hamiltonian can be easily extended to study, for example, the magnetic phases of lattice models coupled to multiple local baths [39]. Second, we identify the phenomenon of decoherence suppression via relaxation, demonstrating it through analytical insights (Eq. (19) and Fig. 3) and supporting it with numerical simulations (Fig. 4).

The paper is organized as follows. In Section II, we introduce our model, consisting of a system coupled to multiple

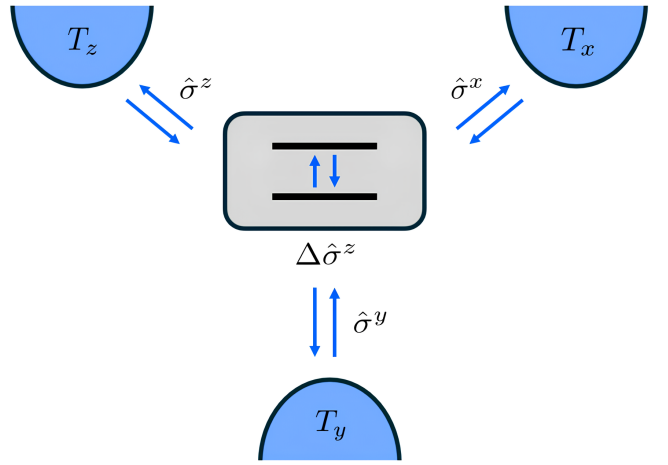


FIG. 1: Scheme of our model: A two-level (qubit) system couples to three independent heat baths through noncommuting operators, $\hat{\sigma}^x$, $\hat{\sigma}^y$, and $\hat{\sigma}^z$. Δ is the spin splitting. Each bath couples to the system with a different strength, characterized by the interaction parameters $\lambda_{x,y,z}$.

For simplicity, we assume that all baths share the same spectral properties with a cutoff frequency Ω and spectral width γ . We also set their temperatures to

$$T = T_x = T_y = T_z.$$

baths through noncommuting operators. We discuss our methods in Sec. III: The Redfield QME in Sec. III A and the RC Markovian embedding method in Sec. III B. In Sec. III C, we provide a brief overview of the EFFH method, highlighting its mathematical formulation and limitations. Predictions based on the EFFH method are included in Sec. IV. Guided by these results, RC-QME simulations are presented in Section V, focusing on the effect of decoherence suppression by increasing the coupling to a dissipative bath. We conclude in Section VI with a summary of our findings.

II. MODEL

We consider a single spin (qubit), characterized by the energy splitting Δ and the tunneling rate E . The system Hamiltonian is given by $\hat{H}_S = \Delta\hat{\sigma}^z + E\hat{\sigma}^x$. This qubit is coupled to two or three independent bosonic baths, indexed by α . Each bath includes a set of harmonic oscillators, indexed by their momentum k . We write the total Hamiltonian in the three-bath case as ($\hbar = 1$),

$$\hat{H} = \Delta\hat{\sigma}^z + E\hat{\sigma}^x + \sum_{\alpha=x,y,z} \sum_k \left[t_{\alpha,k} \hat{\sigma}^\alpha (\hat{c}_{\alpha,k}^\dagger + \hat{c}_{\alpha,k}) + \nu_{\alpha,k} \hat{c}_{\alpha,k}^\dagger \hat{c}_{\alpha,k} \right] \quad (1)$$

Here, $\nu_{\alpha,k}$ and $t_{\alpha,k}$ represent the frequency of the k th mode of the α bath and its coupling strength to the system. We denote the baths by $\alpha = x, y, z$, identifying along which spin orientation they couple to the system. The operators $\hat{c}_{\alpha,k}$ are bosonic annihilation operators of the corresponding mode and

bath. The system's operators \hat{o}^α couple to the displacements of the baths, and are given in terms of the $\alpha = x, y, z$ Pauli matrices. The coupling to the environment can be described by spectral density functions $J^\alpha(\omega) = \sum_k |t_{\alpha,k}|^2 \delta(\omega - \nu_{\alpha,k})$.

We can construct four nontrivial models, denoted by XY, YZ, XZ and XYZ. We refer to each configuration using its bath indices. For example, if the system couples to two baths through its $\{\alpha\} = \{x, y\}$ Pauli components, the model will be referred to as the XY model. In the XYZ model, the qubit couples to three baths, one for each of its spin orientation, as recently discussed in Ref. [50].

In this work, we focus on the XZ model, which represents coupling to both a dissipative bath (x) and a decohering bath (z). We further discuss the Effective Hamiltonian mapping of the XYZ model. It is important to note that we deliberately choose noncommuting coupling operators to the different baths. We refer to this scenario as “frustration”, since the qubit is coupled through different spin components to the different baths, thus missing a “preferred” direction. As we show in Sec. V, this aspect is essential to demonstrate suppression of decoherence dynamics.

III. METHODS

We next summarize the methods we use: the Redfield QME, which is valid only in the weak-coupling regime for Markovian baths; the RC-QME, which employs Markovian embedding to capture strong-coupling effects; and the EFFFH method, which builds on the RC mapping to provide an approximate yet nonperturbative analytical solution.

A. Weak coupling: The Redfield QME

We summarize the Redfield QME here since the RC-QME builds on it. Using the Born-Markov and weak coupling approximations, one can readily obtain the Redfield equation for the dynamics of the reduced density matrix of the system, $\hat{\rho}(t)$. The equation reads [25]

$$\begin{aligned} \frac{d\rho_{mn}(t)}{dt} &= -i\omega_{mn}\rho_{mn}(t) \\ &\quad - \sum_{\alpha,jl} \left\{ R_{mj,jl}^\alpha(\omega_{lj})\rho_{ln}(t) + [R_{nl,lj}^\alpha(\omega_{jl})]^*\rho_{mj}(t) \right. \\ &\quad \left. - [R_{ln,mj}^\alpha(\omega_{jm}) + [R_{jm,nl}^\alpha(\omega_{ln})]^*] \rho_{jl}(t) \right\}. \end{aligned} \quad (2)$$

Here, ω_m are the eigenvalues of the system's Hamiltonian, \hat{H}_S , and $\omega_{mn} = \omega_m - \omega_n$. The upper indices in the Redfield dissipator correspond to a given bath, and the lower indices refer to the matrix elements in the energy eigenbasis of the system's Hamiltonian. In this derivation, the initial state of the total system+baths was written as a tensor product of the system and each individual bath. Importantly, in Eq. (2) the impacts of the different baths are additive and there is no cooperative effect between them. This is reflected in the total dissipator written as the sum of the Redfield tensor of all baths.

The Redfield tensor depends on the matrix elements of the coupling operators and the bath equilibrium correlation functions via

$$R_{mn,jl}^\alpha(\omega) = S_{mn}^\alpha S_{jl}^\alpha \int_0^\infty d\tau e^{i\omega\tau} \langle \hat{B}^\alpha(\tau) \hat{B}^\alpha(0) \rangle. \quad (3)$$

Here, $\hat{B}^\alpha(\tau) = \sum_k t_{\alpha,k} (\hat{c}_{\alpha,k}^\dagger e^{i\nu_{\alpha,k}\tau} + \hat{c}_{\alpha,k} e^{-i\nu_{\alpha,k}\tau})$ is the bath part of the interaction Hamiltonian. \hat{S}^α are the coupled system's operators, which in Eq. (1) are Pauli matrices. To derive this expression, one needs to assume that the baths are stationary. Taking the continuum limit with respect to the momentum degrees of freedom of the baths, and splitting the Redfield tensor into its real and imaginary parts allows us to write

$$R_{mn,jl}^\alpha(\omega) = S_{mn}^\alpha S_{jl}^\alpha [\Gamma^\alpha(\omega) + i\delta^\alpha(\omega)]. \quad (4)$$

The real functions $\Gamma^\alpha(\omega)$ and $\delta^\alpha(\omega)$ are the symmetric part of the correlation function and the lamb shift, respectively. We set the lamb shift equal to zero in our considerations [51]. To compute the real part of the Redfield tensor, the spectral density function of each bath needs to be specified; we choose the Brownian function given by

$$J^\alpha(\omega) = \frac{4\gamma_\alpha\Omega_\alpha^2\lambda_\alpha^2\omega}{(\omega^2 - \Omega_\alpha^2)^2 + (2\pi\gamma_\alpha\Omega_\alpha\omega)^2}. \quad (5)$$

Here, Ω_α corresponds to the peak of the spectral function and γ_α is its width parameter. The parameter λ_α describes the system-bath coupling strength, which in the weak coupling regime has to be the smallest energy scale. As we will see in Section III B, a narrow spectral function is crucial to utilizing the RC-QME, which handles the strong coupling regime of our models.

In terms of the spectral function, the symmetric part of the correlation function is

$$\Gamma^\alpha(\omega) = \begin{cases} \pi J^\alpha(|\omega|)n(|\omega|) & \omega < 0 \\ \pi J^\alpha(\omega)[n(\omega) + 1] & \omega > 0 \\ \lim_{\omega \rightarrow 0} \pi J^\alpha(\omega)n(\omega) & \omega = 0. \end{cases} \quad (6)$$

Here, $n(\omega) = (e^{\beta\omega} - 1)^{-1}$ is the Bose-Einstein distribution function with the inverse temperature $\beta = 1/T$ ($k_B = 1$).

B. Strong coupling: The Reaction Coordinate QME

Beyond the weak system-bath coupling regime, the Born-Markov approximation cannot be justified. A powerful approach to strong coupling is the idea of *Markovian embedding*. The Reaction Coordinate procedure is an example of this framework. It relies on applying a unitary transformation that extracts a degree of freedom from each bath; the extended system is assumed to weakly couple to the rest of the baths' degrees of freedom. A collective degree of freedom extracted from the bath is called a *reaction coordinate*, from which the

transformation takes its name. After the RC mapping, Eq. (1) translates to [44, 52–55]

$$\begin{aligned} \hat{H}^{\text{RC}} = & \Delta \hat{\sigma}^z + \sum_{\alpha} [\Omega_{\alpha} \hat{a}_{\alpha}^{\dagger} \hat{a}_{\alpha} + \lambda_{\alpha} \hat{\sigma}^{\alpha} (\hat{a}_{\alpha}^{\dagger} + \hat{a}_{\alpha})] \\ & + \sum_{\alpha, k} f_{\alpha, k} (\hat{a}_{\alpha}^{\dagger} + \hat{a}_{\alpha}) (\hat{b}_{\alpha, k}^{\dagger} + \hat{b}_{\alpha, k}) + \sum_{\alpha, k} \omega_{\alpha, k} \hat{b}_{\alpha, k}^{\dagger} \hat{b}_{\alpha, k}, \end{aligned} \quad (7)$$

where for simplicity, we set $E = 0$. $\{\hat{a}_{\alpha}\}$ and $\{\hat{b}_{\alpha, k}\}$ are annihilation operators of the extracted reaction coordinates and the residual bath modes, respectively. The new coupling strengths between the reaction coordinate and the residual bath are denoted by $f_{\alpha, k}$. The frequencies and coupling strength of the reaction coordinates are given by Ω_{α} and λ_{α} , respectively. For a general spectral function of the model, we find these parameters using $\lambda_{\alpha}^2 = \frac{1}{\Omega_{\alpha}} \int_0^{\infty} d\omega \omega J^{\alpha}(\omega)$ and $\Omega_{\alpha}^2 = \frac{\int_0^{\infty} d\omega \omega^3 J^{\alpha}(\omega)}{\int_0^{\infty} d\omega \omega J^{\alpha}(\omega)}$ [56]. For the choice of Brownian functions, λ and Ω are the parameters of the original bath as included in Eq. (5).

We refer to the combined system+reaction coordinates as the “extended system”, described by the Hamiltonian,

$$\hat{H}_S^{\text{RC}} = \hat{H}_S + \sum_{\alpha} [\Omega_{\alpha} \hat{a}_{\alpha}^{\dagger} \hat{a}_{\alpha} + \lambda_{\alpha} \hat{\sigma}^{\alpha} (\hat{a}_{\alpha}^{\dagger} + \hat{a}_{\alpha})]. \quad (8)$$

Other terms in Eq. (7) correspond to the interaction between the RCs and the residual bath, and the Hamiltonians of the residual baths. The interaction of an RC with its residual bath is described by the spectral density function $J_{\text{RC}}^{\alpha}(\omega) = \sum_k |f_{k, \alpha}|^2 \delta(\omega - \omega_{\alpha, k})$; there exists a general method to find this new spectral function from the original model [28]. Here, using the Brownian spectral function, we get an ohmic function [54],

$$J_{\text{RC}}^{\alpha}(\omega) = \gamma_{\alpha} \omega e^{-\omega/\Lambda_{\alpha}}, \quad (9)$$

where Λ_{α} is a large energy cutoff and the dimensionless width parameter γ_{α} of Eq. (5) now corresponds to the residual coupling parameter. Assuming small γ_{α} , the extended system weakly couples to the bath. Under the additional assumption of Markovianity for the residual bath, the Redfield QME, Eq. (2), can be used to study the dynamics and steady-state behavior of the extended model at arbitrary λ_{α} , now an intrinsic parameter of the extended Hamiltonian of the system.

To evaluate the Redfield tensor (3), we use the interaction Hamiltonian of the residual baths and identify $\hat{S}^{\alpha} = \hat{a}_{\alpha}^{\dagger} + \hat{a}_{\alpha}$. Expressions for the symmetric part of the correlation function, after the mapping, are obtained from Eq. (6).

C. Strong coupling: Effective Hamiltonian theory

To gain a deeper understanding of the effects of noncommuting couplings to baths on the system’s dynamics, we employ the effective Hamiltonian theory introduced in Ref. [44]. It was recently extended in Ref. [45] to the case of multiple baths with noncommuting coupling operators. The EFFFH

method allows for deriving closed-form system Hamiltonians, which are dressed with functions of the interaction parameters. These functions reveal the impact of the environments on the system. Briefly, using the EFFFH method we (i) extract reaction coordinates from each bath, and (ii) perform a polaron transformation on the reaction coordinates. This transformation weakens the coupling of the RCs to the system while imprinting coupling parameters into the system. (iii) We truncate the spectrum of each RC to its ground state.

Performing the effective mapping of the Hamiltonian in Eq. (1) gives the following formal equation [45],

$$\begin{aligned} \hat{H}^{\text{eff}} = & \Delta (\hat{\sigma}^z)^{\text{eff}} + E (\hat{\sigma}^x)^{\text{eff}} \\ & + \sum_{\alpha} \sum_k \left[\omega_{\alpha, k} \hat{b}_{\alpha, k}^{\dagger} \hat{b}_{\alpha, k} - \frac{2\lambda_{\alpha} f_{\alpha, k}}{\Omega_{\alpha}} (\hat{\sigma}^{\alpha})^{\text{eff}} (\hat{b}_{\alpha, k}^{\dagger} + \hat{b}_{\alpha, k}) \right]. \end{aligned} \quad (10)$$

We omit terms containing \hat{S}_{α}^2 that would normally appear in the effective Hamiltonian [44, 45]. This is because in Eq. (1), \hat{S}^{α} are the Pauli matrices, and the terms with \hat{S}_{α}^2 provide constant energy shifts. The effective system operators are computed using the formula [45]

$$(\hat{\sigma}^{\alpha})^{\text{eff}} = \int \hat{U}_P(\tilde{\mathbf{p}}) \hat{\sigma}^{\alpha} \hat{U}_P^{\dagger}(\tilde{\mathbf{p}}) \prod_{\alpha} \frac{e^{-\tilde{p}_{\alpha}^2}}{\sqrt{\pi}} d\tilde{p}_{\alpha}, \quad (11)$$

where $\tilde{p}_{\alpha} = p_{\alpha}/\sqrt{\Omega_{\alpha}}$ is the renormalized momentum and $\hat{U}_P(\tilde{\mathbf{p}})$ is the polaron transform in the momentum representation,

$$\hat{U}_P(\tilde{\mathbf{p}}) = \exp \left(-i\sqrt{2} \sum_{\alpha} \tilde{p}_{\alpha} \frac{\lambda_{\alpha}}{\Omega_{\alpha}} \hat{\sigma}^{\alpha} \right). \quad (12)$$

In Sec. IV A, we discuss the mapping of the XYZ and XZ models.

The EFFFH method relies on two assumptions about the original baths: (i) The mapping is based on the extraction of reaction coordinates; we assume that the original spectral functions are narrow. Specifically, we use Eq. (5) with $\gamma_{\alpha} \ll 1$. (ii) The spectrum of each RC is truncated, leaving its ground state only. This step relies on the assumption that the reaction coordinate frequency is a large energy scale in the problem. However, previous studies showed that the EFFFH method was in fact accurate and even exact for steady state at the ultra-strong coupling limit, $\lambda_{\alpha} \gg \Omega_{\alpha}$ [44, 46].

IV. PREDICTIONS FROM THE EFFECTIVE HAMILTONIAN MODEL

The dynamics under the Effective Hamiltonian can be studied analytically, to provide closed-form *nonperturbative* expressions for the decoherence and relaxation rates. To derive the decoherence rate under the EFFFH theory, we first present in Sec. IV A the dressing functions that prepare the Effective Hamiltonian; technical details are delegated to Appendix A. Next, turning to the decoherence rate, we present results for

the XZ model in Sec. IV B. Detailed derivations, as well as the analysis of the XYZ model, are included in Appendix B. Guided by the predictions of the EFFH method, which suggest that enhanced coupling to a dissipative bath can suppress decoherence dynamics, we validate these predictions in Section V through RC-QME numerical simulations.

A. Dressing functions

We compute the effective system operators by evaluating Eq. (11) with (12) for the XYZ model, leading to

$$(\hat{\sigma}^\alpha)^{\text{eff}} = \kappa_\alpha(\epsilon_x, \epsilon_y, \epsilon_z) \hat{\sigma}^\alpha. \quad (13)$$

For details, see Appendix A. Here, $\epsilon_\alpha \equiv \lambda_\alpha/\Omega_\alpha$ and $\kappa_\alpha(\epsilon_x, \epsilon_y, \epsilon_z)$ is a dressing function of the operator $\hat{\sigma}^\alpha$; arguments of the dressing functions denote the baths to which the system is coupled. For example, in the XZ model, $\kappa_x(\epsilon_x, \epsilon_z)$ is the dressing function of the operator $\hat{\sigma}^x$. It is significant to note that in our model, the mappings of the Pauli matrices return the same Pauli matrices, only multiplied by functions of the parameters ϵ_α . That is, the effective model does not create new internal terms in the system's Hamiltonian or new coupling terms. As we show in Appendix A, in the XZ model,

we obtain

$$(\hat{\sigma}^\alpha)^{\text{eff}} = \kappa_\alpha(\epsilon_x, \epsilon_z) \hat{\sigma}^\alpha. \quad (14)$$

In our notation, since ϵ_y does not appear in the equation above, it means that it is set to zero. While we focus here on the XZ model, mapping other combinations of system operators leads to identical results, differing only by cyclic permutations,

$$\begin{aligned} \kappa_x(\epsilon_x, \epsilon_z) &= \kappa_y(\epsilon_x, \epsilon_y) = \kappa_z(\epsilon_y, \epsilon_z), \\ \kappa_y(\epsilon_x, \epsilon_z) &= \kappa_z(\epsilon_x, \epsilon_y) = \kappa_x(\epsilon_y, \epsilon_z), \\ \kappa_z(\epsilon_x, \epsilon_z) &= \kappa_x(\epsilon_x, \epsilon_y) = \kappa_y(\epsilon_y, \epsilon_z). \end{aligned} \quad (15)$$

We present the dressing functions of the XZ model in Fig. 2 with the three panels depicting (a) $\kappa_x(\epsilon_x, \epsilon_z)$, (b) $\kappa_y(\epsilon_x, \epsilon_z)$, and (c) $\kappa_z(\epsilon_x, \epsilon_z)$. Beginning in panel (a), we find that $\kappa_x(\epsilon_x, \epsilon_z)$ decreases monotonically as ϵ_z increases, but grows as ϵ_x increases. The complementary behavior is shown in panel (c): $\kappa_z(\epsilon_x, \epsilon_z)$ decreases when increasing ϵ_x , but increases with increasing ϵ_z . These relationships between the dressing functions will be important when we later discuss the decoherence dynamics. As for $\kappa_y(\epsilon_x, \epsilon_z)$ in panel (b), it reaches its upper limit 1 when both ϵ_z and ϵ_x are small (approaching zero). Interestingly, it can also become negative once both ϵ_z and ϵ_x are large. However, in the EFFH theory, κ_y does not impact the decoherence dynamics of the XZ model; thus, we do not dwell on its behavior.

We now write the general form of the Effective Hamiltonian emerging from Eq. (1), by substituting the effective operators into Eq. (10),

$$\hat{H}^{\text{eff}} = \kappa_z(\epsilon_x, \epsilon_y, \epsilon_z) \Delta \hat{\sigma}^z + \kappa_x(\epsilon_x, \epsilon_y, \epsilon_z) E \hat{\sigma}^x + \sum_\alpha \sum_k \omega_{\alpha,k} \hat{b}_{\alpha,k}^\dagger \hat{b}_{\alpha,k} - \sum_\alpha \sum_k 2\epsilon_\alpha \kappa_\alpha(\epsilon_x, \epsilon_y, \epsilon_z) f_{\alpha,k} \hat{\sigma}^\alpha (\hat{b}_{\alpha,k}^\dagger + \hat{b}_{\alpha,k}). \quad (16)$$

The first two terms correspond to \hat{H}_S^{eff} . They describe the mapping of the system's Hamiltonian through renormalization terms to the tunneling energy and the energy gap. The third term describes the residual bath. The last term corresponds to the interaction Hamiltonian between the effective system and the residual baths. We capture this interaction through the coupling of the $\kappa_\alpha(\epsilon_x, \epsilon_y, \epsilon_z) \hat{\sigma}^\alpha$ dressed component of the system to the bosonic displacements of the baths, with the baths' spectral functions

$$J_{\text{eff}}^\alpha(\omega) = (2\epsilon_\alpha)^2 \sum_k |f_{\alpha,k}|^2 \delta(\omega - \omega_{\alpha,k}). \quad (17)$$

Equation (16) clearly illustrates the effects of strong coupling and noncommutativity. Due to strong coupling effects, the system's parameters become dressed as we observe in \hat{H}_S^{eff} . The specific important impact of noncommutative coupling operators is that the interaction of the system with each bath depends on its interaction with other baths, as we see in the κ_α prefactor in the last term of Eq. (16).

B. Decoherence rates

We now focus on the XZ model in which a qubit couples to two baths through its $\hat{\sigma}^x$ and $\hat{\sigma}^z$ operators. Considering the corresponding Effective Hamiltonian, we solve the dynamics using Redfield QME in Appendix B. We find that off-diagonal elements of the reduced density matrix decay exponentially as $\exp[-\Gamma_d t]$ with $\Gamma_d = \Gamma_{\text{eff}}^x/2 + \Gamma_{\text{eff}}^z$ [57]. The $\Gamma_{\text{eff}}^\alpha$ rate results from the coupling of the system to the α bath. However, each rate reflects the impact of the other bath through (i) the renormalization of the system splitting, $\Delta \rightarrow 2\kappa_z(\epsilon_x, \epsilon_z)\Delta$ and (ii) the modification to the system bath coupling through the $\kappa_\alpha(\epsilon_x, \epsilon_z)$ factors. The contribution to the rate due to the x bath is

$$\begin{aligned} \Gamma_{\text{eff}}^x &= 2\pi[\kappa_x(\epsilon_x, \epsilon_z)]^2 J_{\text{eff}}^x(2\kappa_z\Delta)[2n_B(2\kappa_z\Delta) + 1] \\ &\approx 2\pi[\kappa_x(\epsilon_x, \epsilon_z)]^2 4\epsilon_x^2 \gamma_x (2\kappa_z\Delta) [2n_B(2\kappa_z\Delta) + 1] \\ &\xrightarrow{T \gg \kappa_z\Delta} 16\pi[\kappa_x(\epsilon_x, \epsilon_z)]^2 \epsilon_x^2 \gamma_x T. \end{aligned} \quad (18)$$

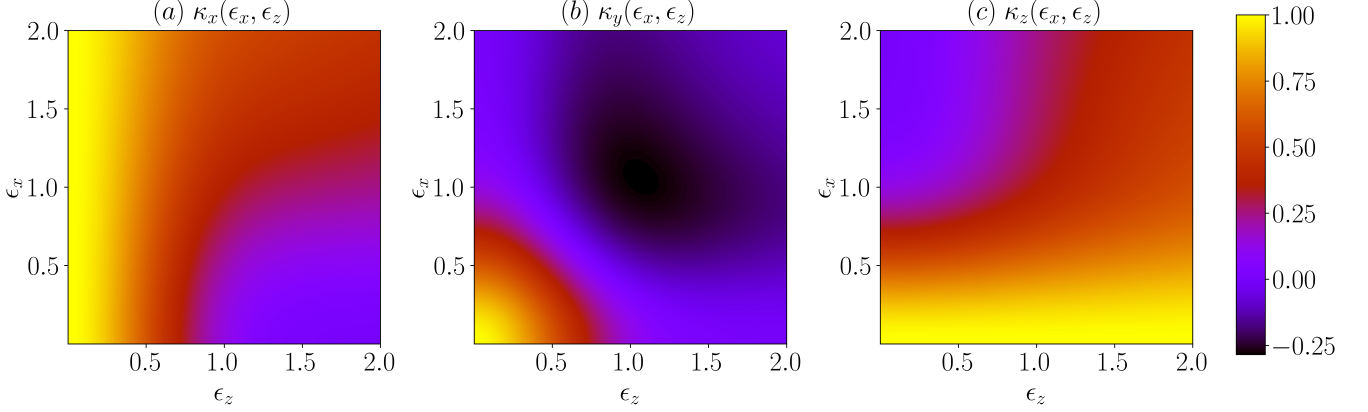


FIG. 2: Effective Hamiltonian theory. Presented are maps of the dressing functions for the XZ model, Eq. (14) with (a) $\kappa_x(\epsilon_x, \epsilon_z)$, (b) $\kappa_y(\epsilon_x, \epsilon_z)$, and (c) $\kappa_z(\epsilon_x, \epsilon_z)$. Maps are plotted with respect to the parameters $\epsilon_\alpha = \lambda_\alpha/\Omega_\alpha$.

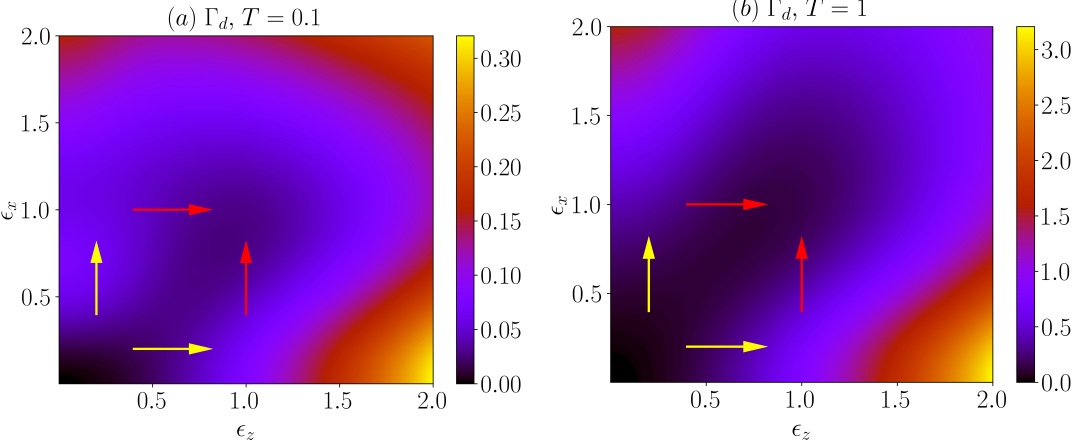


FIG. 3: The decoherence rate constant $\Gamma_d = \Gamma_{\text{eff}}^z + \Gamma_{\text{eff}}^x/2$, based on the Effective Hamiltonian theory, Eqs. (18)-(19), is plotted as a function of the coupling parameters $\epsilon_z = \lambda_z/\Omega_z$ and $\epsilon_x = \lambda_x/\Omega_x$ at (a) $T = 0.1$ and (b) $T = 1$. Other parameters are $\Omega_z = \Omega_x = 8$, $\gamma_z = \gamma_x = \frac{0.05}{\pi}$, $\Delta = 1$. Yellow and red arrows represent paths in the parameter space that cause the decoherence rate to increase and decrease, respectively.

The decoherence rate due to the z bath is

$$\begin{aligned} \Gamma_{\text{eff}}^z &= \lim_{\omega \rightarrow 0} 2\pi J_{\text{eff}}^z(\omega)[2n_B(\omega) + 1] \\ &\approx 16\pi[\kappa_z(\epsilon_x, \epsilon_z)]^2 \epsilon_z^2 \gamma_z T. \end{aligned} \quad (19)$$

For clarity, in this equation and below, we adopt the short notation κ_z for $\kappa_z(\epsilon_x, \epsilon_z)$ when dressing the energy splitting. The approximate sign indicated that we assume large cutoff for the residual bath, $\Lambda \rightarrow \infty$.

We make the following critical observation: The two rates, Γ_{eff}^x and Γ_{eff}^z , which together build the total rate of decoherence, depend each on *both* coupling parameters ϵ_z and ϵ_x . Only in the weak coupling limit, $\kappa_{x,z} \rightarrow 1$ resulting in each rate depending only on the parameters of its bath. This reflects that at weak coupling, there are no cooperative effects between the baths. In contrast, at strong coupling the dressing functions introduce cooperative effects.

In Fig. 3, we present maps of the decoherence rate as a function of ϵ_x and ϵ_z at two different temperatures (identi-

cal for the two baths). The yellow arrows depict the “normal” behavior: When ϵ_z is small, indicating weak coupling to the decohering bath, increasing this coupling, or alternatively growing the coupling to the dissipative (x) bath through enhancing ϵ_x , would make the decoherence rate larger. This is the expected behavior: coupling a qubit more strongly to a decohering bath, or to an additional dissipative environment, should accelerate the decoherence process.

However, when ϵ_z is large (e.g., $\epsilon_z = 1$), we observe the counter, anomalous phenomenon. Here, as we follow the vertical red line, increasing the dissipative coupling through ϵ_x from 0 to say 1.0, *slows down* the decoherence dynamics. Similarly, if we couple the qubit strongly to the x bath and gradually increase ϵ_z , we follow the horizontal red line and observe suppression of the decoherence rate.

We can explain these normal and anomalous trends based on Eqs. (18)-(19). The decoherence rate Γ_d is given by the sum of $\Gamma_{\text{eff}}^x/2$ and Γ_{eff}^z . When ϵ_z is small, Γ_d is dominated

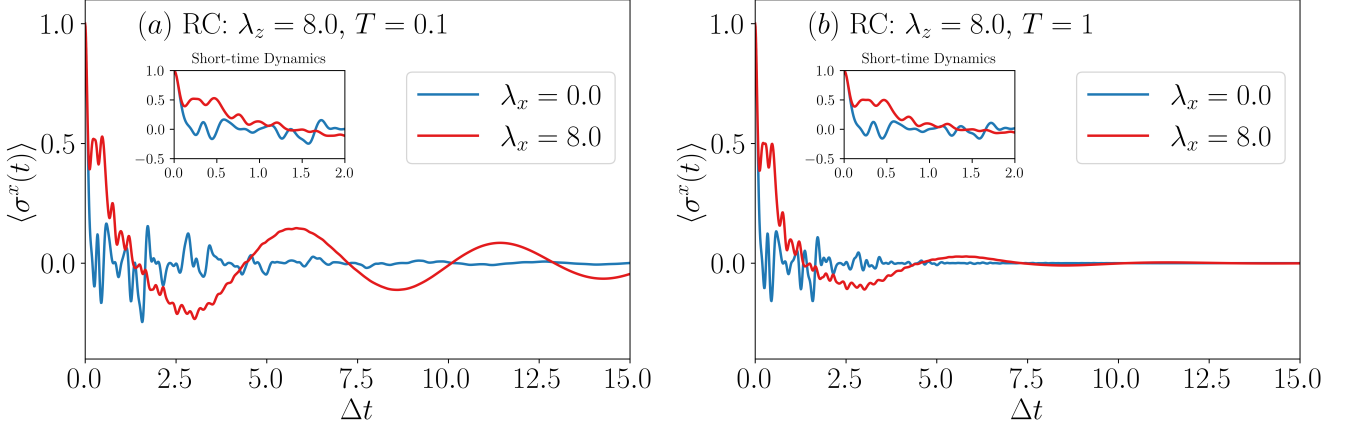


FIG. 4: RC-QME simulations of decoherence dynamics at temperatures (a) $T = 0.1$ and (b) $T = 1$ at strong coupling to the decohering bath, $\lambda_z = 8$. We present results at $\lambda_x = 0$ (blue) and $\lambda_x = 8$ (red). Other parameters are $\Omega_{x,z} = 8$, $\Delta = 1$, $\gamma_{x,z} = 0.05/\pi$. We truncate the two RCs, and use $M = 5$ levels to represent each of them. The insets focus on the short time dynamics up to $\Delta t = 2$.

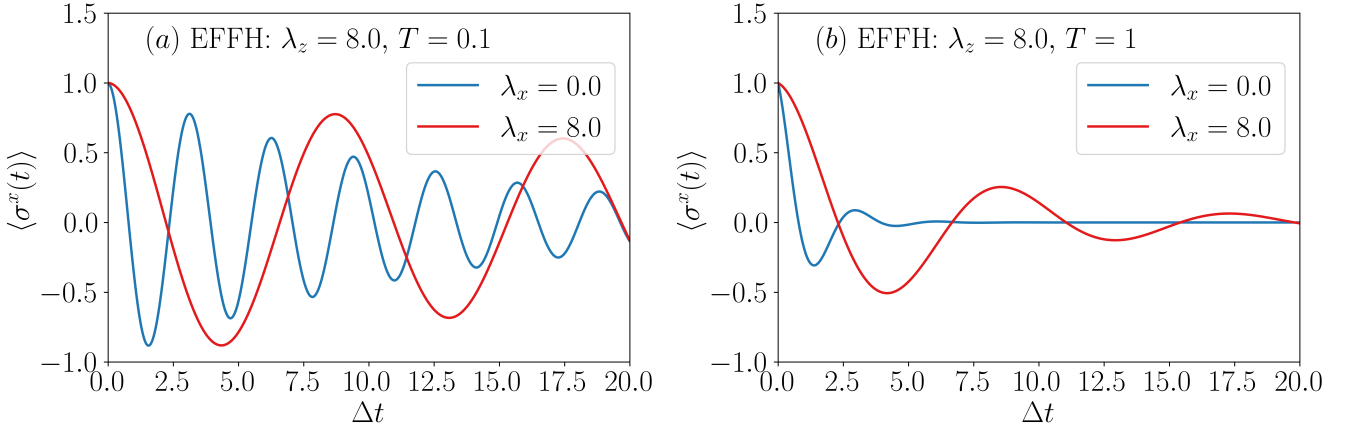


FIG. 5: EFFH-QME simulations of decoherence dynamics at temperatures (a) $T = 0.1$ and (b) $T = 1$ at strong coupling to the decohering bath, $\lambda_z = 8$. We present results at $\lambda_x = 0$ (blue) and $\lambda_x = 8$ (red). Other parameters are the same as in Fig. 4.

by $\Gamma_{\text{eff}}^x \propto \epsilon_x^2 \kappa_x^2$ (note that we assume high temperature in this discussion, such that we approximate $n_B(\omega) \approx T/\omega$). As we increase ϵ_x , moving along the vertical yellow line, the decoherence rate increases due to the quadratic dependence ϵ_x^2 ; the factor κ_x does not change much with ϵ_x when ϵ_z is small, see Fig. 2(a). This explains the normal trend of enhanced decoherence with increasing coupling to the dissipative bath. In contrast, when ϵ_z is large, Γ_d is dominated by $\Gamma_{\text{eff}}^z \propto \epsilon_z^2 \kappa_z^2$. In this limit, an increase in ϵ_x suppresses κ_z as we see in Fig. 2(c), leading to an overall decrease in the decoherence rate, captured by the red vertical line. This effect is anomalous to common expectations regarding decoherence.

The suppression of decoherence by enhanced dissipation takes place at different temperatures, as shown in Fig. 3 (a)-(b). Furthermore, based on Eqs. (18)-(19) and the argument above, we expect it to hold even when the baths are maintained at different temperatures.

Another interesting prediction from the EFFH theory is that

we can identify scenarios in which *both* decoherence and relaxation rates can be simultaneously suppressed by enhanced coupling. As shown in Appendix B, the population relaxation rate is only determined by Γ_{eff}^x , while the decoherence rate is given by the sum $\Gamma_{\text{eff}}^x/2 + \Gamma_{\text{eff}}^z$. At large ϵ_x , increasing ϵ_z suppresses κ_x , which, since $\Gamma_{\text{eff}}^x \propto \epsilon_x^2 \kappa_x^2$, dominates both population relaxation and decoherence rates. Following the red horizontal line in Fig. 3, we expect both effects to be suppressed in this regime.

Complementing these results, in Appendix B we solve the dynamics of the Effective Hamiltonian using the Redfield QME. We also introduce an additional bath coupled via the $\hat{\sigma}^y$ operator. We show that the decoherence rate is then determined by $(\Gamma_{\text{eff}}^x + \Gamma_{\text{eff}}^y + 2\Gamma_{\text{eff}}^z)/2$. Consequently, the parameters $\epsilon_x, \epsilon_y, \epsilon_z$ all influence the overall decoherence rate, and a similar cooperative effect can be expected.

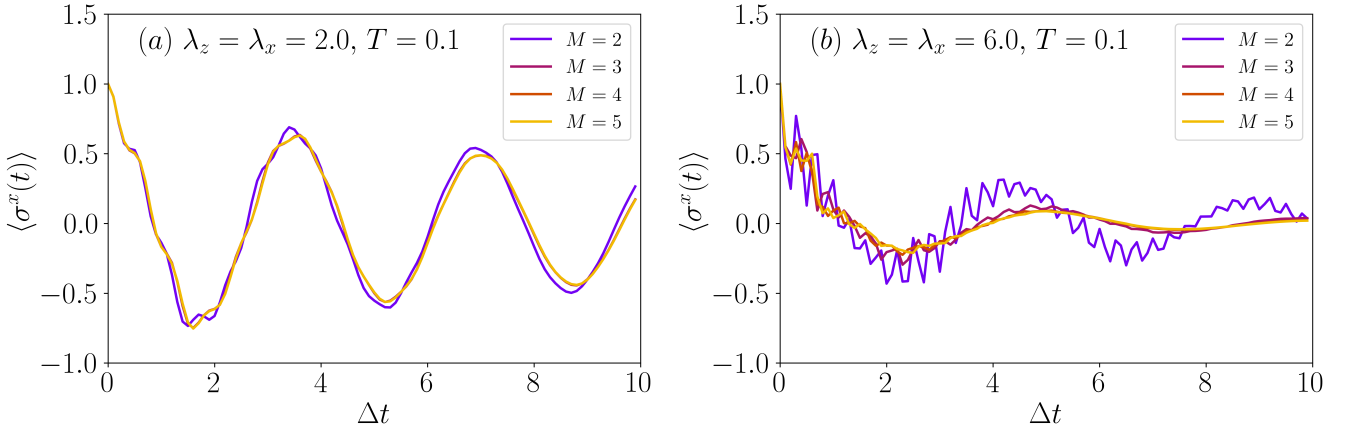


FIG. 6: Convergence tests for the RC-QME simulations. We present the coherences adopting different number of RC levels, M . We perform tests at (a) weak and (b) strong coupling to both baths.

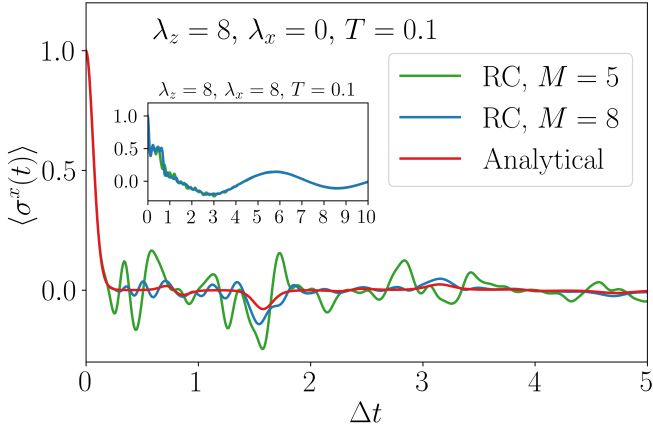


FIG. 7: Convergence tests for Fig. 4. Comparison of the dynamics of coherences using exact-analytical and RC-QME simulations with $M = 5$ and $M = 8$. The exact-analytical solution, valid at $\lambda_z = 0$ is given in Eq. (20) [24]. Main: Convergence test for $\lambda_x = 0$, $\lambda_z = 8$. Inset: Convergence test for $\lambda_x = 8$, $\lambda_z = 8$. Other physical parameters are as in Fig. 4 with $T = 0.1$.

V. RC-QME SIMULATIONS

A. Suppression of decoherence rate

Guided by the predictions of the EFFH theory, we now present simulations using the RC-QME method. These results are expected to be accurate for narrow spectral functions $\gamma_\alpha \ll 1$; a small γ_α implies weak system-residual bath coupling. Our chosen simulation parameters are $\Omega_z = \Omega_x = 8$, $\gamma_z = \gamma_x = 0.05/\pi$, $\Delta = 1$, which we keep fixed across all simulations unless otherwise stated. For the initial condition, we use $\rho_{11} = 0.5$ and $\rho_{12} = 0.5$ for the qubit, where 1 and 2 denote the ground state and excited state of the qubit and ρ stands for the reduced density matrix of the system. The initial condi-

tion of the RC is thermal with respect to the attached bath. In the figures below, we present $\langle \sigma^x(t) \rangle = \rho_{12}(t) + \rho_{21}(t)$ as a function of time in dimensionless units, Δt .

Fig. 4 presents our main result: The suppression of decoherence by dissipation. In this example, we strongly couple the qubit to the decohering bath with $\lambda_z = 8$, which, with $\Omega_z = 8$ corresponds to $\epsilon_z = 1$. In the absence of coupling to the dissipative bath, the decoherence dynamics is rapid, with coherences decaying essentially to zero at very short timescales (blue line); we discuss the subsequent rapid oscillations of the dynamics in Fig. 7. However, when we introduce the coupling to the dissipative bath, $\lambda_x \neq 0$, the decoherence process slows significantly (red). This phenomenon is illustrated at two different temperatures in Fig. 4(a)-(b). As expected, the decoherence process is faster at high temperatures, but similarly to the low temperature case, increasing the coupling λ_x helps mitigating it.

How does the EFFH method perform? The decoherence dynamics predicted by the EFFH method, when solved using the Redfield QME, are presented in Fig. 5. Comparing these results to RC-QME results from Fig. 4, we find that the EFFH method is only qualitatively correct for these parameters. While the absolute values in the two figures differ, the overall trend of suppressing decoherence dynamics due to a strong λ_x coupling remains consistent.

B. Convergence tests

To validate our main result in Fig. 4, we performed several convergence and benchmarking tests. First, in Fig. 6, we examine the convergence of the RC-QME simulations with respect to the truncation of the RC modes. Here, M denotes the number of levels included for each RC. At weak coupling to the baths, Fig. 6(a) shows that good convergence is already achieved at $M = 3$. However, at strong coupling, Fig. 6(b) demonstrates that more levels ($M = 5$) are necessary for convergence. Notably, this figure exhibits a “normal” decoherence behavior: As the coupling to the dissipative bath

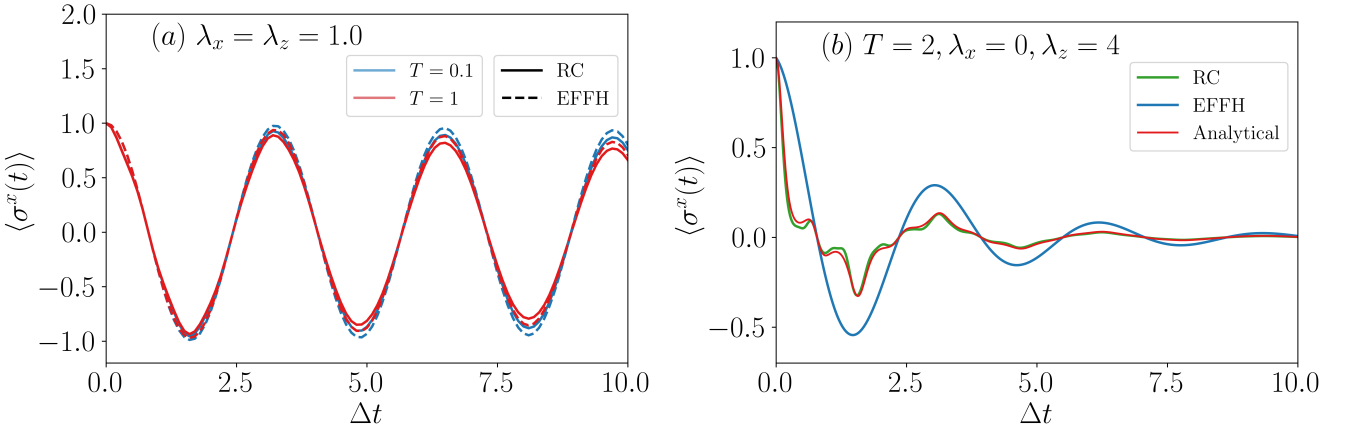


FIG. 8: Coherence dynamics at (a) weak and (b) intermediate coupling strength to the baths. (a) In the weak dissipative limit, EFFH-QME simulations well agree with RC-QME results. Parameters are $T = 0.1$ and $T = 0.1$ with $\lambda_{x,z} = 1$. (b) In the pure decoherence model and beyond weak coupling, $\lambda_z = 4$, we compare RC-QME, EFFH-QME and analytical results at $T = 2$ showing qualitative correct trends of the EFFH method.

increases, we observe a corresponding increase in the decoherence rate when comparing panels (a) and (b).

To further investigate the accuracy of the RC-QME simulations of Fig. 4, we analyze the coherence dynamics in a pure decoherence model in the strong coupling regime ($\lambda_z = 8$, $\lambda_x = 0$), comparing the RC-QME results to the exact analytical solution [24],

$$\begin{aligned} \Gamma(t) &= -4 \int_0^\infty d\omega J^z(\omega) \coth\left(\frac{\beta\omega}{2}\right) \frac{1 - \cos\omega t}{\omega^2}, \\ \langle \sigma^x(t) \rangle &= e^{\Gamma(t)} \cos(2\Delta t). \end{aligned} \quad (20)$$

Here $J^z(\omega)$ is defined as in Eq. 5. Fig. 7 shows that as we increase M from five to eight levels, the rapid oscillations up to $\Delta t = 5$ are suppressed, and we get closer to the exact solution. The fast and spiky oscillations of the pure decoherence dynamics in Fig. 4 are thus the outcome of the truncation of the RC manifold, as we also observed in Ref. [29]. In the inset of Fig. 7, we present a convergence test for the strong-coupling regime with $\lambda_{x,z} = 8$. Interestingly, in this case, the convergence is already quite robust for $M = 5$. Thus, while in our parameters it is challenging to converge the pure decoherence dynamics with the RC-QME, the general case with both baths active can be feasibly simulated.

We further compare EFFH-QME to RC-QME simulations in Fig. 8. In the weak coupling limit, Fig. 8(a) shows that the EFFH method well captures the RC-QME simulations, though decoherence is minimal. As we increase the coupling energy to the moderate regime, Fig. 8(b) demonstrates that the EFFH method captures essential features of the dynamics: the oscillation frequency and coherence lifetime. This highlights the usefulness of the EFFH predictions. Further increasing the coupling, Fig. 5 shows deviations from Fig. 4 as mentioned above, yet capturing qualitative trends.

Finally, we note that we benchmarked RC-QME results against numerically exact calculations with the Hierarchical Equations of Motion in Refs. [46, 58], using similar param-

eters as we used here. There, we confirmed the accuracy of the RC-QME simulations for both dynamics and steady state values.

VI. CONCLUSIONS

We studied the decoherence dynamics of a qubit coupled to multiple baths through its noncommuting operators. After presenting our methods, we first applied the EFFH framework on our model. This approach enabled us to derive closed-form analytic expressions for the decoherence rate beyond the weak coupling regime, providing insights into strategies for mitigating decoherence. The resulting decoherence rate constant (the inverse of the T_2 timescale) revealed how the decoherence dynamics depended on noncommutativity and coupling strengths: It demonstrated bath cooperativity and exposed conditions under which decoherence suppression may occur.

Guided by the EFFH predictions, we performed numerical simulations using the RC-QME method. When the system was weakly coupled to both the decohering and the dissipative baths, the system exhibited a normal behavior: The decoherence rate increased as either coupling strength was increased. In contrast, at strong coupling to the decohering bath, increasing the qubit's coupling to a dissipative bath slowed down the decoherence process, defying conventional expectations.

Our results relied on the noncommutativity of the coupling operators; the nontrivial impact of noncommuting coupling operators on quantum dynamics is gaining increasing attention across various applications. The suppression of population relaxation due to increasing interaction with an additional bath was previously discussed in Refs. [45, 48, 49, 59, 60]. A related phenomenon: the enhancement of entanglement between a qubit and its three environments when coupled through different spin components was explored in Ref. 50. In

Ref. [61], it was shown that when a system couples via non-commuting operators to both Markovian and non-Markovian baths, the presence of the Markovian environment can render the interaction with the non-Markovian bath effectively memoryless.

Coupling a system via its noncommuting operators to non-Markovian baths at strong coupling is particularly relevant in plasmonic light-matter setups. For example, this scenario applies for describing the dynamics of molecular quantum emitters in lossy nanocavities while also interacting with an intramolecular vibrational bath [62, 63]. Another area of significant impact are quantum processors, where control architectures are designed to improve the T_1 and T_2 lifetimes. Our work here, alongside Ref. 45, suggests that frustration effects can serve as a mechanism to mitigate noise, which is supported by recent experiments [60]. A significant strength of our study lies in the analytical EFFH framework we develop, which provides guidelines on controlling open quantum system dynamics in complex settings, across a broad range of coupling regimes, multiple baths, and with noncommuting interaction operators. Our results also have implications on the performance of qubit-based thermal conductors [64] and thermal machines [35, 65, 66], and the study of whether they can be optimized in the transient or steady-state regime with

strong coupling when using noncommuting baths.

With regard to future prospects, we hope that our study inspires experimental efforts to verify our predictions and implement this strategy for designing quantum systems with long-lived coherences. On the theoretical side, various computational approaches, particularly numerically exact methods [67, 68], could be employed to further investigate the suppression of population relaxation and decoherence dynamics through cooperative effects. It is also interesting to examine our model using other mapping approaches, such as the pseudo mode method [69]. Finally, our framework can be readily extended beyond single impurities to large spins and to lattice models with local couplings to multiple vibrational modes.

ACKNOWLEDGMENTS

D.S. acknowledges support from an NSERC Discovery Grant. This research has been funded in part by the research project: “Quantum Software Consortium: Exploring Distributed Quantum Solutions for Canada” (QSC). QSC is financed under the National Sciences and Engineering Research Council of Canada (NSERC) Alliance Consortia Quantum Grants #ALLRP587590-23.

Appendix A: Derivation of the effective Hamiltonian models

This Appendix is dedicated to evaluating the effective operators from the general formula Eq. (11). We use the polaron operators (12) and derive the dressing functions in Eq. (13) and (14). For simplicity, we omit here the tilde notation for the renormalized momenta, $\tilde{p}_\alpha \rightarrow p_\alpha$. We also use the notation $\epsilon_\alpha = \lambda_\alpha/\Omega_\alpha$.

1. XZ model

We begin by deriving the expressions for the effective system operators in the XZ model. The polaron transformation is

$$\hat{U}_P(\mathbf{p}) = \hat{\sigma}^0 \cos \left(\sqrt{2} \sqrt{p_x^2 \epsilon_x^2 + p_z^2 \epsilon_z^2} \right) - \frac{i \sin \left(\sqrt{2} \sqrt{p_x^2 \epsilon_x^2 + p_z^2 \epsilon_z^2} \right)}{\sqrt{p_x^2 \epsilon_x^2 + p_z^2 \epsilon_z^2}} \left(\hat{\sigma}^x p_x \epsilon_x + \hat{\sigma}^z p_z \epsilon_z \right). \quad (\text{A1})$$

We obtain the effective system operators as integrals over the renormalized momenta,

$$\begin{aligned} (\hat{\sigma}^x)^{\text{eff}} &= \int \frac{d\mathbf{p}}{\pi} \left(\hat{\sigma}^x \frac{p_z^2 \epsilon_z^2 \cos \left(2\sqrt{2} \sqrt{p_x^2 \epsilon_x^2 + p_z^2 \epsilon_z^2} \right) + p_x^2 \epsilon_x^2}{p_x^2 \epsilon_x^2 + p_z^2 \epsilon_z^2} + \hat{\sigma}^y \frac{p_z \epsilon_z \sin \left(2\sqrt{2} \sqrt{p_x^2 \epsilon_x^2 + p_z^2 \epsilon_z^2} \right)}{\sqrt{p_x^2 \epsilon_x^2 + p_z^2 \epsilon_z^2}} \right. \\ &\quad \left. - \hat{\sigma}^z \frac{2p_x p_z \epsilon_x \epsilon_z \sin^2 \left(\sqrt{2} \sqrt{p_x^2 \epsilon_x^2 + p_z^2 \epsilon_z^2} \right)}{p_x^2 \epsilon_x^2 + p_z^2 \epsilon_z^2} \right) \\ &= \hat{\sigma}^x \int \frac{d\mathbf{p}}{\pi} \frac{p_z^2 \epsilon_z^2 \cos \left(2\sqrt{2} \sqrt{p_x^2 \epsilon_x^2 + p_z^2 \epsilon_z^2} \right) + p_x^2 \epsilon_x^2}{p_x^2 \epsilon_x^2 + p_z^2 \epsilon_z^2}, \end{aligned} \quad (\text{A2})$$

$$\begin{aligned}
(\hat{\sigma}^y)^{\text{eff}} &= \int \frac{d\mathbf{p}}{\pi} \left(-\hat{\sigma}^x \frac{p_z \epsilon_z \sin(2\sqrt{2}\sqrt{p_x^2 \epsilon_x^2 + p_z^2 \epsilon_z^2})}{\sqrt{p_x^2 \epsilon_x^2 + p_z^2 \epsilon_z^2}} + \hat{\sigma}^y \cos(2\sqrt{2}\sqrt{p_x^2 \epsilon_x^2 + p_z^2 \epsilon_z^2}) \right. \\
&\quad \left. + \hat{\sigma}^z \frac{p_x \epsilon_x \sin(2\sqrt{2}\sqrt{p_x^2 \epsilon_x^2 + p_z^2 \epsilon_z^2})}{\sqrt{p_x^2 \epsilon_x^2 + p_z^2 \epsilon_z^2}} \right) \\
&= \hat{\sigma}^y \int \frac{d\mathbf{p}}{\pi} \cos(2\sqrt{2}\sqrt{p_x^2 \epsilon_x^2 + p_z^2 \epsilon_z^2}),
\end{aligned} \tag{A3}$$

$$\begin{aligned}
(\hat{\sigma}^z)^{\text{eff}} &= \int \frac{d\mathbf{p}}{\pi} \left(\hat{\sigma}^x \frac{2p_x p_z \epsilon_x \epsilon_z \sin^2(\sqrt{2}\sqrt{p_x^2 \epsilon_x^2 + p_z^2 \epsilon_z^2})}{p_x^2 \epsilon_x^2 + p_z^2 \epsilon_z^2} - \hat{\sigma}^y \frac{p_x \epsilon_x \sin(2\sqrt{2}\sqrt{p_x^2 \epsilon_x^2 + p_z^2 \epsilon_z^2})}{\sqrt{p_x^2 \epsilon_x^2 + p_z^2 \epsilon_z^2}} \right. \\
&\quad \left. + \hat{\sigma}^z \frac{p_x^2 \epsilon_x^2 \cos(2\sqrt{2}\sqrt{p_x^2 \epsilon_x^2 + p_z^2 \epsilon_z^2}) + p_z^2 \epsilon_z^2}{p_x^2 \epsilon_x^2 + p_z^2 \epsilon_z^2} \right) \\
&= \hat{\sigma}^z \int \frac{d\mathbf{p}}{\pi} \frac{p_x^2 \epsilon_x^2 \cos(2\sqrt{2}\sqrt{p_x^2 \epsilon_x^2 + p_z^2 \epsilon_z^2}) + p_z^2 \epsilon_z^2}{p_x^2 \epsilon_x^2 + p_z^2 \epsilon_z^2}.
\end{aligned} \tag{A4}$$

Here we introduce the notation $\int \frac{d\mathbf{p}}{\pi} = \frac{1}{\pi} \int_{-\infty}^{\infty} dp_x \int_{-\infty}^{\infty} dp_z e^{-p_x^2 - p_z^2}$. To compute the effective system operators, we substitute $p_x \rightarrow r \cos(\theta)$, $p_z \rightarrow r \sin(\theta)$ and obtain

$$\begin{aligned}
(\hat{\sigma}^x)^{\text{eff}} &= \hat{\sigma}^x \int_0^\infty \frac{e^{-r^2} r}{\pi} dr \int_0^{2\pi} d\theta \frac{\sin^2(\theta) \epsilon_z^2 \cos(2\sqrt{2}r \sqrt{\cos^2(\theta) \epsilon_x^2 + \sin^2(\theta) \epsilon_z^2}) + \cos^2(\theta) \epsilon_x^2}{\cos^2(\theta) \epsilon_x^2 + \sin^2(\theta) \epsilon_z^2} \\
&\equiv \hat{\sigma}^x \kappa_x(\epsilon_x, \epsilon_z) = \hat{\sigma}^x h(\epsilon_x, \epsilon_z),
\end{aligned} \tag{A5}$$

$$\begin{aligned}
(\hat{\sigma}^y)^{\text{eff}} &= \hat{\sigma}^y \int_0^\infty \frac{e^{-r^2} r}{\pi} dr \int_0^{2\pi} d\theta \cos(2\sqrt{2}r \sqrt{\cos^2(\theta) \epsilon_x^2 + \sin^2(\theta) \epsilon_z^2}) \\
&\equiv \hat{\sigma}^y \kappa_y(\epsilon_x, \epsilon_z) = \hat{\sigma}^y f(\epsilon_x, \epsilon_z),
\end{aligned} \tag{A6}$$

$$\begin{aligned}
(\hat{\sigma}^z)^{\text{eff}} &= \hat{\sigma}^z \int_0^\infty \frac{e^{-r^2} r}{\pi} dr \int_0^{2\pi} d\theta \frac{\cos^2(\theta) \epsilon_x^2 \cos(2\sqrt{2}r \sqrt{\cos^2(\theta) \epsilon_x^2 + \sin^2(\theta) \epsilon_z^2}) + \sin^2(\theta) \epsilon_z^2}{\cos^2(\theta) \epsilon_x^2 + \sin^2(\theta) \epsilon_z^2} \\
&\equiv \hat{\sigma}^z \kappa_z(\epsilon_x, \epsilon_z) = \hat{\sigma}^z g(\epsilon_x, \epsilon_z).
\end{aligned} \tag{A7}$$

We introduce here three integral dressing functions of two arguments, f , g , and h . It turns out that three dressing functions show up for systems with other combinations of two-bath coupling operators, dressing different operators.

In case where $\forall \alpha \epsilon_\alpha = \epsilon$ the integral functions simplify and can be expressed in terms of the Dawson integral function F ,

$$\begin{aligned}
h(\epsilon) &= g(\epsilon) = 1 - \sqrt{2}\epsilon F(\sqrt{2}\epsilon), \\
f(\epsilon) &= 1 - 2\sqrt{2}\epsilon F(\sqrt{2}\epsilon).
\end{aligned} \tag{A8}$$

2. XYZ model

In the XYZ model, each bath couples to the system via the operators $\hat{\sigma}^x$, $\hat{\sigma}^y$ and $\hat{\sigma}^z$. The polaron transform is

$$\hat{U}_P(\mathbf{p}) = \begin{pmatrix} \cos(\sqrt{2}E(\mathbf{p}, \epsilon)) - \frac{ip_z \epsilon_z \sin(\sqrt{2}E(\mathbf{p}, \epsilon))}{E(\mathbf{p}, \epsilon)} & \frac{(-p_y \epsilon_y - ip_x \epsilon_x) \sin(\sqrt{2}E(\mathbf{p}, \epsilon))}{E(\mathbf{p}, \epsilon)} \\ \frac{(p_y \epsilon_y - ip_x \epsilon_x) \sin(\sqrt{2}E(\mathbf{p}, \epsilon))}{E(\mathbf{p}, \epsilon)} & \cos(\sqrt{2}E(\mathbf{p}, \epsilon)) + \frac{ip_z \epsilon_z \sin(\sqrt{2}E(\mathbf{p}, \epsilon))}{E(\mathbf{p}, \epsilon)} \end{pmatrix}, \tag{A9}$$

where here $E(\mathbf{p}, \epsilon) = \sqrt{p_x^2 \epsilon_x^2 + p_y^2 \epsilon_y^2 + p_z^2 \epsilon_z^2}$. We use a coordinate transformation given by $p_x = r \sin(\theta) \cos(\phi)$, $p_y = r \sin(\theta) \sin(\phi)$, $p_z = r \cos(\theta)$ and get

$$\hat{U}_P(r, \theta, \phi) = \begin{pmatrix} \cos(r\sqrt{2}D(\theta, \phi, \epsilon)) - \frac{i \cos(\theta) \epsilon_z \sin(r\sqrt{2}D(\theta, \phi, \epsilon))}{D(\theta, \phi, \epsilon)} & \frac{\sin(\theta)(-\epsilon_y \sin(\phi) - i \epsilon_x \cos(\phi)) \sin(r\sqrt{2}D(\theta, \phi, \epsilon))}{D(\theta, \phi, \epsilon)} \\ \frac{\sin(\theta)(\epsilon_y \sin(\phi) - i \epsilon_x \cos(\phi)) \sin(r\sqrt{2}D(\theta, \phi, \epsilon))}{D(\theta, \phi, \epsilon)} & \cos(r\sqrt{2}D(\theta, \phi, \epsilon)) + \frac{i \cos(\theta) \epsilon_z \sin(r\sqrt{2}D(\theta, \phi, \epsilon))}{D(\theta, \phi, \epsilon)} \end{pmatrix}, \quad (\text{A10})$$

where $D(\theta, \phi, \epsilon) = \sqrt{\sin^2(\theta) (\epsilon_x^2 \cos^2(\phi) + \epsilon_y^2 \sin^2(\phi)) + \cos^2(\theta) \epsilon_z^2}$. If all couplings are identical, $\epsilon_\alpha = \epsilon$ the polaron operator simplifies to

$$\hat{U}_P(r, \theta, \phi) = \begin{pmatrix} \cos(\sqrt{2}r\epsilon) - i \cos(\theta) \sin(\sqrt{2}r\epsilon) & \sin(\theta) \sin(\sqrt{2}r\epsilon) (-\sin(\phi) - i \cos(\phi)) \\ \sin(\theta) \sin(\sqrt{2}r\epsilon) (\sin(\phi) - i \cos(\phi)) & \cos(\sqrt{2}r\epsilon) + i \cos(\theta) \sin(\sqrt{2}r\epsilon) \end{pmatrix}. \quad (\text{A11})$$

In this special limit, we find that for all system operators are dressed according to

$$\begin{aligned} (\hat{\sigma}^\alpha)^{\text{eff}} &= \hat{\sigma}^\alpha \int_0^\infty dr \int_0^\pi d\theta \int_0^{2\pi} d\phi \frac{r^2 e^{-r^2} \sin(\theta)}{\pi^{3/2}} \left(\cos(2\theta) \sin^2(\sqrt{2}r\epsilon) + \cos^2(\sqrt{2}r\epsilon) \right) \\ &= \hat{\sigma}^\alpha \left[\frac{2}{3} e^{-2\epsilon^2} (1 - 4\epsilon^2) + \frac{1}{3} \right]. \end{aligned} \quad (\text{A12})$$

Returning to the general interaction model, the effective operators are given by the following integral functions,

$$\begin{aligned} (\hat{\sigma}^x)^{\text{eff}} &= \hat{\sigma}^x \int \frac{d\mathbf{p}}{\pi^{3/2}} \frac{(p_z^2 \epsilon_z^2 + p_y^2 \epsilon_y^2) \cos(2\sqrt{2} \sqrt{p_x^2 \epsilon_x^2 + p_y^2 \epsilon_y^2 + p_z^2 \epsilon_z^2}) + p_x^2 \epsilon_x^2}{p_x^2 \epsilon_x^2 + p_y^2 \epsilon_y^2 + p_z^2 \epsilon_z^2}, \\ (\hat{\sigma}^y)^{\text{eff}} &= \hat{\sigma}^y \int \frac{d\mathbf{p}}{\pi^{3/2}} \frac{(p_x^2 \epsilon_x^2 + p_z^2 \epsilon_z^2) \cos(2\sqrt{2} \sqrt{p_x^2 \epsilon_x^2 + p_y^2 \epsilon_y^2 + p_z^2 \epsilon_z^2}) + p_y^2 \epsilon_y^2}{p_x^2 \epsilon_x^2 + p_y^2 \epsilon_y^2 + p_z^2 \epsilon_z^2}, \\ (\hat{\sigma}^z)^{\text{eff}} &= \hat{\sigma}^z \int \frac{d\mathbf{p}}{\pi^{3/2}} \frac{(p_x^2 \epsilon_x^2 + p_y^2 \epsilon_y^2) \cos(2\sqrt{2} \sqrt{p_x^2 \epsilon_x^2 + p_y^2 \epsilon_y^2 + p_z^2 \epsilon_z^2}) + p_z^2 \epsilon_z^2}{p_x^2 \epsilon_x^2 + p_y^2 \epsilon_y^2 + p_z^2 \epsilon_z^2}, \end{aligned} \quad (\text{A13})$$

where we introduce the short notation $\int \frac{d\mathbf{p}}{\pi^{3/2}} = \frac{1}{\pi^{3/2}} \int_{-\infty}^\infty dp_x \int_{-\infty}^\infty dp_y \int_{-\infty}^\infty dp_z e^{-p_x^2 - p_y^2 - p_z^2}$. We already omitted terms that are odd functions of the momenta since they do will not contribute to the integrals. In spherical coordinates we get

$$\begin{aligned} (\hat{\sigma}^x)^{\text{eff}} &= \hat{\sigma}^x \int_0^\infty r^2 dr \int_0^\pi \sin(\theta) d\theta \int_0^{2\pi} d\phi \frac{e^{-r^2}}{\pi^{3/2}} I(\theta, \phi, \epsilon_z, \epsilon_y, \epsilon_x) \\ &= \hat{\sigma}^x \kappa_x(\epsilon_x, \epsilon_y, \epsilon_z), \\ (\hat{\sigma}^y)^{\text{eff}} &= \hat{\sigma}^y \int_0^\infty r^2 dr \int_0^\pi \sin(\theta) d\theta \int_0^{2\pi} d\phi \frac{e^{-r^2}}{\pi^{3/2}} I(\theta, \phi, \epsilon_x, \epsilon_z, \epsilon_y) \\ &= \hat{\sigma}^y \kappa_y(\epsilon_x, \epsilon_y, \epsilon_z), \\ (\hat{\sigma}^z)^{\text{eff}} &= \hat{\sigma}^z \int_0^\infty r^2 dr \int_0^\pi \sin(\theta) d\theta \int_0^{2\pi} d\phi \frac{e^{-r^2}}{\pi^{3/2}} I(\theta, \phi, \epsilon_y, \epsilon_x, \epsilon_z) \\ &= \hat{\sigma}^z \kappa_z(\epsilon_x, \epsilon_y, \epsilon_z), \end{aligned} \quad (\text{A14})$$

where

$$\begin{aligned} I(\theta, \phi, x, y, z) &= \\ \frac{\sin^2(\theta) (x^2 \cos^2(\phi) + y^2 \sin^2(\phi)) \cos(2r\sqrt{2 \sin^2(\theta) (x^2 \cos^2(\phi) + y^2 \sin^2(\phi)) + 2 \cos^2(\theta) z^2}) + \cos^2(\theta) z^2}{\sin^2(\theta) (x^2 \cos^2(\phi) + y^2 \sin^2(\phi)) + \cos^2(\theta) z^2}. \end{aligned} \quad (\text{A15})$$

To express the momenta integrals in spherical coordinates we used a different coordinate transformation for each operator, namely

$$\begin{aligned} \hat{\sigma}^x : p_y &\rightarrow r \sin(\theta) \cos(\phi), \quad p_z \rightarrow r \sin(\theta) \sin(\phi), \quad p_x \rightarrow r \cos(\theta), \\ \hat{\sigma}^y : p_x &\rightarrow r \sin(\theta) \cos(\phi), \quad p_z \rightarrow r \sin(\theta) \sin(\phi), \quad p_y \rightarrow r \cos(\theta), \\ \hat{\sigma}^z : p_x &\rightarrow r \sin(\theta) \cos(\phi), \quad p_y \rightarrow r \sin(\theta) \sin(\phi), \quad p_z \rightarrow r \cos(\theta). \end{aligned} \quad (\text{A16})$$

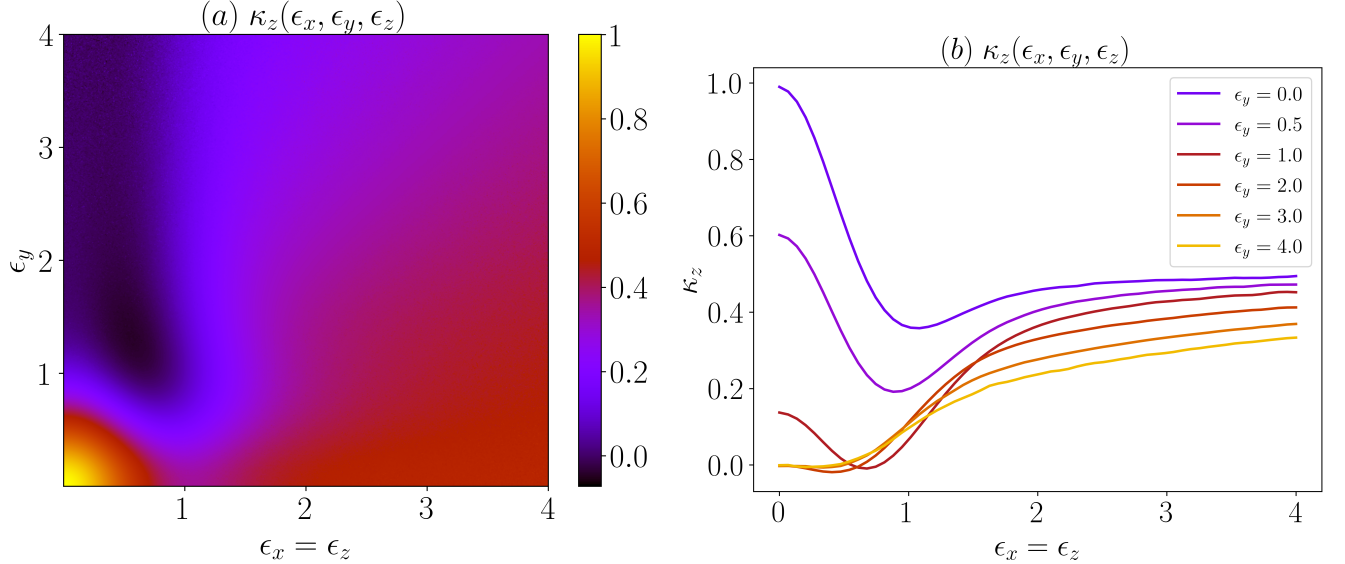


FIG. 9: (a) Surface plot of the function dressing the σ^z operator in the XYZ model for $\epsilon_x = \epsilon_z$. (b) Examples of $\kappa_z(\epsilon_x, \epsilon_y, \epsilon_z)$ with respect to $\epsilon_x = \epsilon_z$ for different values of ϵ_y .

In Fig. 9, we present cuts of the dressing functions when the system is coupled to all three baths, each with a different Pauli matrix. Given the three-dimensional nature of the plots, which depend on $\epsilon_x, \epsilon_y, \epsilon_z$, we provide in Fig. 9(a) a two-dimensional surface plot representing the intersection of the full plot at $\epsilon_x = \epsilon_z$. Additionally, in Fig. 9(b), we present a series of curves showing $\kappa_z(\epsilon_x, \epsilon_y, \epsilon_z)$ values as $\epsilon_x = \epsilon_z$ varies for different ϵ_y values. We find that for small ϵ_y , κ_z initially decreases and then increases slightly as $\epsilon_x = \epsilon_z$ increases. In contrast, at large ϵ_y , κ_z increases monotonically with increasing $\epsilon_x = \epsilon_z$. In addition, at small $\epsilon_x = \epsilon_z$, κ_z vary significantly when increasing ϵ_y . However, at large $\epsilon_x = \epsilon_z$, κ_z approaches a constant value, independent of ϵ_y .

Appendix B: Dynamics under the Effective Hamiltonian model using the Redfield QME

In this Appendix, we solve the Redfield equation for the reduced density matrix for Effective Hamiltonian models introduced in Section IV.

1. XZ model

Applying the general Redfield equation Eq. (2) together with Eq. (4) and Eq. (6) on the Effective Hamiltonian, Eq. (16), and reducing it to the XZ model, we get equations of motion for the coherences and population.

a. Coherences

The dynamics of coherences is given by

$$\begin{aligned}
\dot{\rho}_{12}(t) &= -i\omega_{12}\rho_{12}(t) \\
&\quad + \left[-R_{11,11}^z(\omega_{11}) - R_{22,22}^{z,*}(\omega_{22}) + R_{22,11}^z(\omega_{11}) + R_{11,22}^{z,*}(\omega_{22}) \right] \rho_{12}(t) \\
&\quad - \left[R_{12,21}^x(\omega_{12}) + R_{21,12}^{x,*}(\omega_{21}) \right] \rho_{12}(t) + \left[R_{12,12}^x(\omega_{21}) + R_{21,21}^{x,*}(\omega_{12}) \right] \rho_{21}(t) \\
&= -i\omega_{12}\rho_{12}(t) \\
&\quad - \left[2\pi (\kappa_z^{xz})^2 J_{\text{eff}}^z(0)(2n_B(0) + 1) \right] \rho_{12}(t) \\
&\quad - \left[\pi (\kappa_x^{xz})^2 J_{\text{eff}}^x(\omega_{21})(2n_B(\omega_{21}) + 1) \right] \rho_{12}(t) + \left[\pi (\kappa_x^{xz})^2 J_{\text{eff}}^x(\omega_{21})(2n_B(\omega_{21}) + 1) \right] \rho_{21}(t).
\end{aligned} \tag{B1}$$

We use the compact notation $\kappa_\alpha^{xz} = \kappa_\alpha(\epsilon_x, \epsilon_z)$ with the baths to which the system is coupled indicated as superscripts of κ . We also denote the qubit levels by 1 (ground) and 2 (excited), thus $\omega_{21} = -\omega_{12} = 2\kappa_z^{xz}\Delta$. We now identify two rate constants,

$$\begin{aligned}
\Gamma_{\text{eff}}^x &= 2\pi (\kappa_x^{xz})^2 J_{\text{eff}}^x(2\kappa_z^{xz}\Delta)(2n_B(2\kappa_z^{xz}\Delta) + 1) \\
&\approx 2\pi (\kappa_x^{xz})^2 (4\epsilon_x^2 \gamma_x) \times (2\kappa_z^{xz}\Delta)(2n_B(2\kappa_z^{xz}\Delta) + 1) \\
&\xrightarrow{T \gg \kappa_z^{xz}\Delta} 16\pi (\kappa_x^{xz})^2 \epsilon_x^2 \gamma_x T,
\end{aligned} \tag{B2}$$

and

$$\begin{aligned}
\Gamma_{\text{eff}}^z &= \lim_{\omega \rightarrow 0} 2\pi (\kappa_z^{xz})^2 J_{\text{eff}}^z(\omega)(2n_B(\omega) + 1) \\
&\approx 2\pi (\kappa_z^{xz})^2 4\epsilon_z^2 \frac{2\gamma_z}{\beta} \\
&= 16\pi (\kappa_z^{xz})^2 \epsilon_z^2 \gamma_z T.
\end{aligned} \tag{B3}$$

We use the approximate sign as we work in the high cutoff limit of Eq. (9). This allows us to write the equations of motion in a compact form,

$$\begin{aligned}
\dot{\rho}_{12}(t) &= -i\omega_{12}\rho_{12}(t) - \Gamma_{\text{eff}}^z\rho_{12}(t) - \frac{1}{2}\Gamma_{\text{eff}}^x\rho_{12}(t) + \frac{1}{2}\Gamma_{\text{eff}}^x\rho_{21}(t), \\
\dot{\rho}_{21}(t) &= i\omega_{12}\rho_{21}(t) - \Gamma_{\text{eff}}^z\rho_{21}(t) - \frac{1}{2}\Gamma_{\text{eff}}^x\rho_{21}(t) + \frac{1}{2}\Gamma_{\text{eff}}^x\rho_{12}(t).
\end{aligned} \tag{B4}$$

In a matrix form,

$$\begin{pmatrix} \dot{\rho}_{12}(t) + \dot{\rho}_{21}(t) \\ \dot{\rho}_{12}(t) - \dot{\rho}_{21}(t) \end{pmatrix} = \begin{pmatrix} -\Gamma_{\text{eff}}^z & i\omega_{21} \\ i\omega_{21} & -\Gamma_{\text{eff}}^z - \Gamma_{\text{eff}}^x \end{pmatrix} \begin{pmatrix} \rho_{12}(t) + \rho_{21}(t) \\ \rho_{12}(t) - \rho_{21}(t) \end{pmatrix} \tag{B5}$$

The eigenvalues of the matrix in the above equation are determined from the characteristic equation,

$$(-\Gamma_{\text{eff}}^z - \lambda)(-\Gamma_{\text{eff}}^z - \Gamma_{\text{eff}}^x - \lambda) = (i\omega_{21})^2, \tag{B6}$$

leading to

$$\lambda_{\pm} = \frac{-(2\Gamma_{\text{eff}}^z + \Gamma_{\text{eff}}^x) \pm \sqrt{(\Gamma_{\text{eff}}^x)^2 - 4\omega_{21}^2}}{2}. \tag{B7}$$

The corresponding eigenvectors are

$$\vec{v}_+ = \begin{pmatrix} 1 \\ \frac{\Gamma_{\text{eff}}^x - \sqrt{(\Gamma_{\text{eff}}^x)^2 - 4\omega_{21}^2}}{2\omega_{21}} \cdot i \end{pmatrix}, \quad \vec{v}_- = \begin{pmatrix} 1 \\ \frac{\Gamma_{\text{eff}}^x + \sqrt{(\Gamma_{\text{eff}}^x)^2 - 4\omega_{21}^2}}{2\omega_{21}} \cdot i \end{pmatrix} \tag{B8}$$

The solution to (B5) is

$$\begin{pmatrix} \rho_{12}(t) + \rho_{21}(t) \\ \rho_{12}(t) - \rho_{21}(t) \end{pmatrix} = c_+ e^{\lambda_+ t} \begin{pmatrix} 1 \\ \frac{\Gamma_{\text{eff}}^x - \sqrt{(\Gamma_{\text{eff}}^x)^2 - 4\omega_{21}^2}}{2\omega_{21}} \cdot i \end{pmatrix} + c_- e^{\lambda_- t} \begin{pmatrix} 1 \\ \frac{\Gamma_{\text{eff}}^x + \sqrt{(\Gamma_{\text{eff}}^x)^2 - 4\omega_{21}^2}}{2\omega_{21}} \cdot i \end{pmatrix}, \tag{B9}$$

with the coefficients c_{\pm} determined by the initial conditions. We use

$$\rho(0) = \frac{1}{2} \begin{pmatrix} 1 & 1 \\ 1 & 1 \end{pmatrix} \quad (\text{B10})$$

and get

$$c_+ = \frac{1}{2} + \frac{\Gamma_{\text{eff}}^x}{4i\theta}, \quad c_- = \frac{1}{2} - \frac{\Gamma_{\text{eff}}^x}{4i\theta} \quad (\text{B11})$$

where $4\theta^2 = -(\Gamma_{\text{eff}}^x)^2 + 4\omega_{21}^2$, and we assume that $\theta > 0$. Putting it together, the off diagonal elements evolve as

$$\begin{aligned} \rho_{12}(t) &= \frac{1}{2} e^{-\frac{t}{2}(\Gamma_{\text{eff}}^x + 2\Gamma_{\text{eff}}^z)} \left[\cos(\theta t) + \frac{\Gamma_{\text{eff}}^x}{2\theta} \sin(\theta t) + i \frac{\omega_{21}}{\theta} \sin(\theta t) \right], \\ \rho_{21}(t) &= \frac{1}{2} e^{-\frac{t}{2}(\Gamma_{\text{eff}}^x + 2\Gamma_{\text{eff}}^z)} \left[\cos(\theta t) + \frac{\Gamma_{\text{eff}}^x}{2\theta} \sin(\theta t) - i \frac{\omega_{21}}{\theta} \sin(\theta t) \right]. \end{aligned} \quad (\text{B12})$$

Finally, we identify the decoherence rate by $\Gamma_d = \Gamma_{\text{eff}}^x/2 + \Gamma_{\text{eff}}^z$.

b. Population

We write now the Redfield equations of motion for the population, $\rho_{11}(t)$ and $\rho_{22}(t) = 1 - \rho_{11}(t)$. We get

$$\begin{aligned} \dot{\rho}_{11}(t) &= - [R_{12,21}^x(\omega_{12}) + R_{12,21}^{x,*}(\omega_{12})] \rho_{11}(t) + [R_{21,12}^x(\omega_{21}) + R_{21,12}^{x,*}(\omega_{21})] \rho_{22}(t) \\ &= - \left[2\pi (\kappa_x^{xz})^2 J_{\text{eff}}^x(\omega_{21}) n_B(\omega_{21}) \right] \rho_{11}(t) + \left[2\pi (\kappa_x^{xz})^2 J_{\text{eff}}^x(\omega_{21}) (n_B(\omega_{21}) + 1) \right] \rho_{22}(t) \\ &= - \left[2\pi (\kappa_x^{xz})^2 J_{\text{eff}}^x(\omega_{21}) (2n_B(\omega_{21}) + 1) \right] \rho_{11}(t) + \left[2\pi (\kappa_x^{xz})^2 J_{\text{eff}}^x(\omega_{21}) (n_B(\omega_{21}) + 1) \right]. \end{aligned} \quad (\text{B13})$$

Adopting the definition of Γ_{eff}^x of Eq. (B2), we have

$$\begin{aligned} \dot{\rho}_{11}(t) &= -\Gamma_{\text{eff}}^x \rho_{11}(t) + \Gamma_{\text{eff}}^x \frac{n_B(\omega_{21}) + 1}{2n_B(\omega_{21}) + 1}, \\ \dot{\rho}_{22}(t) &= -\Gamma_{\text{eff}}^x \rho_{22}(t) + \Gamma_{\text{eff}}^x \frac{n_B(\omega_{21})}{2n_B(\omega_{21}) + 1}. \end{aligned} \quad (\text{B14})$$

Based on the initial condition, $\rho_{11} = \rho_{22} = \frac{1}{2}$, the solution for the population is

$$\begin{aligned} \rho_{11}(t) &= \left(\frac{1}{2} - \frac{e^{\beta\omega_{21}}}{e^{\beta\omega_{21}} + 1} \right) e^{-\Gamma_{\text{eff}}^x t} + \frac{e^{\beta\omega_{21}}}{e^{\beta\omega_{21}} + 1}, \\ \rho_{22}(t) &= \left(-\frac{1}{2} + \frac{e^{\beta\omega_{21}}}{e^{\beta\omega_{21}} + 1} \right) e^{-\Gamma_{\text{eff}}^x t} + \frac{1}{e^{\beta\omega_{21}} + 1}. \end{aligned} \quad (\text{B15})$$

Clearly, in the long time dynamics, the system thermalizes to the temperature $1/\beta$.

2. XYZ model

Applying the general Redfield equation Eq. (2) together with Eq. (4) and Eq. (6) on the Effective Hamiltonian, Eq. (16), we get equations of motion for the coherences and population.

a. Coherences

The coherences evolve according to

$$\begin{pmatrix} \dot{\rho}_{12} + \dot{\rho}_{21} \\ \dot{\rho}_{12} - \dot{\rho}_{21} \end{pmatrix} = \begin{pmatrix} -\Gamma_{\text{eff}}^z - \Gamma_{\text{eff}}^y & i\omega_{21} \\ i\omega_{21} & -\Gamma_{\text{eff}}^z - \Gamma_{\text{eff}}^x \end{pmatrix} \begin{pmatrix} \rho_{12}(t) + \rho_{21}(t) \\ \rho_{12}(t) - \rho_{21}(t) \end{pmatrix}, \quad (\text{B16})$$

where

$$\begin{aligned}
\Gamma_{\text{eff}}^x &= 2\pi (\kappa_x^{xyz})^2 J_{\text{eff}}^x(2\kappa_z^{xyz}\Delta)(2n_B(2\kappa_z^{xyz}\Delta) + 1) \\
&\approx 2\pi (\kappa_x^{xyz})^2 4\epsilon_x^2 \gamma_x 2\kappa_z^{xyz} \Delta (2n_B(2\kappa_z^{xyz}\Delta) + 1) \\
&\xrightarrow{T \gg \kappa_z^{xyz}\Delta} 16\pi (\kappa_x^{xyz})^2 \epsilon_x^2 \gamma_x T, \\
\Gamma_{\text{eff}}^y &= 2\pi (\kappa_y^{xyz})^2 J_{\text{eff}}^y(2\kappa_z^{xyz}\Delta)(2n_B(2\kappa_z^{xyz}\Delta) + 1) \\
&\approx 2\pi (\kappa_y^{xyz})^2 4\epsilon_y^2 \gamma_y 2\kappa_z^{xyz} \Delta (2n_B(2\kappa_z^{xyz}\Delta) + 1) \\
&\xrightarrow{T \gg \kappa_z^{xyz}\Delta} 16\pi (\kappa_y^{xyz})^2 \epsilon_y^2 \gamma_y T, \\
\Gamma_{\text{eff}}^z &= \lim_{\omega \rightarrow 0} 2\pi (\kappa_z^{xyz})^2 J_{\text{eff}}^z(\omega)(2n_B(\omega) + 1) \\
&\approx 2\pi (\kappa_z^{xyz})^2 4\epsilon_z^2 \frac{2\gamma_z}{\beta} \\
&= 16\pi (\kappa_z^{xyz})^2 \epsilon_z^2 \gamma_z T.
\end{aligned} \tag{B17}$$

where $\kappa_\alpha^{xyz} = \kappa_\alpha(\epsilon_x, \epsilon_y, \epsilon_z)$. We use the approximate sign since we work in the Λ -large limit of Eq. (9). Using the initial condition (B10), we get

$$\begin{pmatrix} \dot{\rho}_{12} + \dot{\rho}_{21} \\ \dot{\rho}_{12} - \dot{\rho}_{21} \end{pmatrix} = e^{-\frac{t}{2}(\Gamma_{\text{eff}}^x + \Gamma_{\text{eff}}^y + 2\Gamma_{\text{eff}}^z)} \begin{pmatrix} \cos(\theta t) + \frac{(\Gamma_{\text{eff}}^x - \Gamma_{\text{eff}}^y)}{2\theta} \sin(\theta t) \\ i\frac{\omega_{21}}{\theta} \sin(\theta t) \end{pmatrix}, \tag{B18}$$

where $4\theta^2 = -(\Gamma_{\text{eff}}^x - \Gamma_{\text{eff}}^y)^2 + 4\omega_{21}^2$, and we assume that $\theta > 0$. Separately, the coherence dynamics is given by

$$\begin{aligned}
\rho_{12}(t) &= \frac{1}{2} e^{-\frac{t}{2}(\Gamma_{\text{eff}}^x + \Gamma_{\text{eff}}^y + 2\Gamma_{\text{eff}}^z)} \left[\cos(\theta t) + \frac{\Gamma_{\text{eff}}^x - \Gamma_{\text{eff}}^y}{2\theta} \sin(\theta t) + \frac{i\omega_{21}}{\theta} \sin(\theta t) \right], \\
\rho_{21}(t) &= \frac{1}{2} e^{-\frac{t}{2}(\Gamma_{\text{eff}}^x + \Gamma_{\text{eff}}^y + 2\Gamma_{\text{eff}}^z)} \left[\cos(\theta t) + \frac{\Gamma_{\text{eff}}^x - \Gamma_{\text{eff}}^y}{2\theta} \sin(\theta t) - \frac{i\omega_{21}}{\theta} \sin(\theta t) \right].
\end{aligned} \tag{B19}$$

b. Population

For population dynamics we get

$$\begin{aligned}
\rho_{11}(t) &= \left(\frac{1}{2} - \frac{e^{\beta\omega_{21}}}{e^{\beta\omega_{21}} + 1} \right) e^{-(\Gamma_{\text{eff}}^x + \Gamma_{\text{eff}}^y)t} + \frac{e^{\beta\omega_{21}}}{e^{\beta\omega_{21}} + 1}, \\
\rho_{22}(t) &= \left(-\frac{1}{2} + \frac{e^{\beta\omega_{21}}}{e^{\beta\omega_{21}} + 1} \right) e^{-(\Gamma_{\text{eff}}^x + \Gamma_{\text{eff}}^y)t} + \frac{1}{e^{\beta\omega_{21}} + 1}.
\end{aligned} \tag{B20}$$

In the XZ model, the population decay rate is proportional to Γ_{eff}^x . As such, stronger coupling to the decohering bath slows down the relaxation dynamics, as κ_x^{xz} is suppressed with increasing ϵ_z [45]. In the XYZ or XY models, the decay rate is proportional to $\Gamma_{\text{eff}}^x + \Gamma_{\text{eff}}^y$, meaning that both κ_x and κ_y contribute. The dressing functions exhibit opposing effects, making the influence of one bath's coupling on the relaxation rate non-monotonic, with the behavior depending on the coupling strength of the other bath(s). In such cases, similar trends to the decoherence dynamics in the XZ model can be expected. As discussed in this work, when the system is strongly coupled to one bath, increasing the coupling to another bath coupled through a noncommuting operator can slow down the decay process.

- [1] Dieter Suter and Gonzalo A. Álvarez, “Colloquium: Protecting quantum information against environmental noise,” *Rev. Mod. Phys.* **88**, 041001 (2016).
[2] Alexander Streltsov, Gerardo Adesso, and Martin B. Plenio,

- “Colloquium: Quantum coherence as a resource,” *Rev. Mod. Phys.* **89**, 041003 (2017).
[3] Ashley Montanaro, “Quantum algorithms: an overview,” *npj Quantum Information* **2**, 15023 (2016).

- [4] Vittorio Giovannetti, Seth Lloyd, and Lorenzo Maccone, “Advances in quantum metrology,” *Nature Photonics* **5**, 222–229 (2011).
- [5] Valentín Zapatero, Tim van Leent, Rotem Arnon-Friedman, *et al.*, “Advances in device-independent quantum key distribution,” *npj Quantum Information* **9**, 10 (2023).
- [6] Moshe Shapiro and Paul Brumer, *Quantum Control of Molecular Processes* (John Wiley & Sons, 2012).
- [7] Chanelle C Jumper, Shahnawaz R. Rather, Siwei Wang, and Gregory D Scholes, “From coherent to vibronic light harvesting in photosynthesis,” *Current Opinion in Chemical Biology* **47**, 39–46 (2018).
- [8] John Preskill, “Quantum Computing in the NISQ era and beyond,” *Quantum* **2**, 79 (2018).
- [9] Sitan Chen, Jordan Cotler, Hsin-Yuan Huang, and Jerry Li, “The complexity of NISQ,” **14**, 6001, publisher: Nature Publishing Group.
- [10] Colin D. Bruzewicz, John Chiaverini, Robert McConnell, and Jeremy M. Sage, “Trapped-ion quantum computing: Progress and challenges,” *Applied Physics Reviews* **6**, 021314 (2019).
- [11] Lorenza Viola and Seth Lloyd, “Dynamical suppression of decoherence in two-state quantum systems,” *Phys. Rev. A* **58**, 2733–2744 (1998).
- [12] Lorenza Viola, Emanuel Knill, and Seth Lloyd, “Dynamical decoupling of open quantum systems,” *Phys. Rev. Lett.* **82**, 2417–2421 (1999).
- [13] Götz S. Uhrig, “Keeping a quantum bit alive by optimized π -pulse sequences,” *Phys. Rev. Lett.* **98**, 100504 (2007).
- [14] Jonas Bylander, Simon Gustavsson, Fei Yan, Fumiki Yoshihara, Khalil Harrabi, George Fitch, David G. Cory, Yasunobu Nakamura, Jaw-Shen Tsai, and William D. Oliver, “Noise spectroscopy through dynamical decoupling with a superconducting flux qubit,” *Nature Physics* **7**, 565–570 (2011).
- [15] Nic Ezzell, Bibek Pokharel, Lina Tewala, Gregory Quiroz, and Daniel A. Lidar, “Dynamical decoupling for superconducting qubits: A performance survey,” *Phys. Rev. Appl.* **20**, 064027 (2023).
- [16] S. Motlakunta, N. Kotibhaskar, C. Y. Shih, and et al., “Preserving a qubit during state-destroying operations on an adjacent qubit at a few micrometers distance,” *Nature Communications* **15**, 6575 (2024).
- [17] Winton Brown and Omar Fawzi, “Decoupling with random quantum circuits,” *Communications in Mathematical Physics* **340**, 867–900 (2015).
- [18] P. Facchi, S. Tasaki, S. Pascazio, H. Nakazato, A. Tokuse, and D. A. Lidar, “Control of decoherence: Analysis and comparison of three different strategies,” *Phys. Rev. A* **71**, 022302 (2005).
- [19] R. Schmidt, A. Negretti, J. Ankerhold, T. Calarco, and J. T. Stockburger, “Optimal control of open quantum systems: Cooperative effects of driving and dissipation,” *Phys. Rev. Lett.* **107**, 130404 (2011).
- [20] D Home and MAB Whitaker, “A conceptual analysis of quantum zeno; paradox, measurement, and experiment,” *Annals of Physics* **258**, 237–285 (1997).
- [21] A. M. Steane, “Error correcting codes in quantum theory,” *Phys. Rev. Lett.* **77**, 793–797 (1996).
- [22] Philipp Treutlein, Theodor W. Hänsch, Jakob Reichel, Antonio Negretti, Markus A. Cirone, and Tommaso Calarco, “Microwave potentials and optimal control for robust quantum gates on an atom chip,” *Phys. Rev. A* **74**, 022312 (2006).
- [23] A. G. Kofman and G. Kurizki, “Unified theory of dynamically suppressed qubit decoherence in thermal baths,” *Phys. Rev. Lett.* **93**, 130406 (2004).
- [24] H.-P. Breuer and F. Petruccione, *The Theory of Open Quantum Systems* (Oxford University Press, 2007).
- [25] A. Nitzan, *Chemical Dynamics in Condensed Phases: Relaxation, Transfer, and Reactions in Condensed Molecular Systems*, Oxford Graduate Texts (OUP Oxford, 2013).
- [26] Keith H. Hughes, Clara D. Christ, and Irene Burghardt, “Effective-mode representation of non-Markovian dynamics: A hierarchical approximation of the spectral density. I. Application to single surface dynamics,” *The Journal of Chemical Physics* **131**, 024109 (2009).
- [27] Keith H. Hughes, Clara D. Christ, and Irene Burghardt, “Effective-mode representation of non-Markovian dynamics: A hierarchical approximation of the spectral density. II. Application to environment-induced nonadiabatic dynamics,” *The Journal of Chemical Physics* **131**, 124108 (2009).
- [28] Ahsan Nazir and Gernot Schaller, “The reaction coordinate mapping in quantum thermodynamics,” in *Thermodynamics in the Quantum Regime: Fundamental Aspects and New Directions*, edited by Felix Binder, Luis A. Correa, Christian Gogolin, Janet Anders, and Gerardo Adesso (Springer International Publishing, Cham, 2018) pp. 551–577.
- [29] Nicholas Anto-Sztrikacs and Dvira Segal, “Capturing non-markovian dynamics with the reaction coordinate method,” *Phys. Rev. A* **104**, 052617 (2021).
- [30] Jake Iles-Smith, Arend G. Dijkstra, Neill Lambert, and Ahsan Nazir, “Energy transfer in structured and unstructured environments: Master equations beyond the born-markov approximations,” *The Journal of Chemical Physics* **144**, 044110 (2016).
- [31] Camille L. Latune, “Steady state in strong system-bath coupling regime: Reaction coordinate versus perturbative expansion,” *Phys. Rev. E* **105**, 024126 (2022).
- [32] Philipp Strasberg, Gernot Schaller, Neill Lambert, and Tobias Brandes, “Nonequilibrium thermodynamics in the strong coupling and non-markovian regime based on a reaction coordinate mapping,” *New Journal of Physics* **18**, 073007 (2016).
- [33] David Newman, Florian Mintert, and Ahsan Nazir, “Performance of a quantum heat engine at strong reservoir coupling,” *Phys. Rev. E* **95**, 032139 (2017).
- [34] Nicholas Anto-Sztrikacs, Felix Ivander, and Dvira Segal, “Quantum thermal transport beyond second order with the reaction coordinate mapping,” *The Journal of Chemical Physics* **156**, 214107 (2022).
- [35] Felix Ivander, Nicholas Anto-Sztrikacs, and Dvira Segal, “Strong system-bath coupling effects in quantum absorption refrigerators,” *Phys. Rev. E* **105**, 034112 (2022).
- [36] Luis A. Correa, Buqing Xu, Benjamin Morris, and Gerardo Adesso, “Pushing the limits of the reaction-coordinate mapping,” *The Journal of Chemical Physics* **151**, 094107 (2019).
- [37] Mike Shubrook, Jake Iles-Smith, and Ahsan Nazir, “Non-markovian quantum heat statistics with the reaction coordinate mapping,” (2024), arXiv:2408.08829 [quant-ph].
- [38] Graeme Pleasance and Francesco Petruccione, “Nonequilibrium quantum heat transport between structured environments,” *New Journal of Physics* **26**, 073025 (2024).
- [39] Brett Min, Nicholas Anto-Sztrikacs, Marlon Brenes, and Dvira Segal, “Bath-engineering magnetic order in quantum spin chains: An analytic mapping approach,” *Phys. Rev. Lett.* **132**, 266701 (2024).
- [40] Philipp Strasberg, Gernot Schaller, Thomas L. Schmidt, and Massimiliano Esposito, “Fermionic reaction coordinates and their application to an autonomous maxwell demon in the strong-coupling regime,” *Phys. Rev. B* **97**, 205405 (2018).
- [41] Sebastian Restrepo, Sina Böhling, Javier Cerrillo, and Gernot Schaller, “Electron pumping in the strong coupling and non-markovian regime: A reaction coordinate mapping approach,”

- Phys. Rev. B* **100**, 035109 (2019).
- [42] Tilmann Ehrlich and Gernot Schaller, “Broadband frequency filters with quantum dot chains,” *Phys. Rev. B* **104**, 045424 (2021).
- [43] Conor McConnell and Ahsan Nazir, “Strong coupling in thermoelectric nanojunctions: a reaction coordinate framework,” *New Journal of Physics* **24**, 025002 (2022).
- [44] Nicholas Anto-Sztrikacs, Ahsan Nazir, and Dvira Segal, “Effective-hamiltonian theory of open quantum systems at strong coupling,” *PRX Quantum* **4**, 020307 (2023).
- [45] Jakub Garwoła and Dvira Segal, “Open quantum systems with noncommuting coupling operators: An analytic approach,” *Phys. Rev. B* **110**, 174304 (2024).
- [46] Nicholas Anto-Sztrikacs, Brett Min, Marlon Brenes, and Dvira Segal, “Effective hamiltonian theory: An approximation to the equilibrium state of open quantum systems,” *Phys. Rev. B* **108**, 115437 (2023).
- [47] Brett Min, Kartiek Agarwal, and Dvira Segal, “Role of bath-induced many-body interactions in the dissipative phases of the su-schrieffer-heeger model,” *Phys. Rev. B* **110**, 125415 (2024).
- [48] Henry Maguire, Jake Iles-Smith, and Ahsan Nazir, “Environmental nonadditivity and franck-condon physics in nonequilibrium quantum systems,” *Phys. Rev. Lett.* **123**, 093601 (2019).
- [49] T. Palm and P. Nalbach, “Suppressing relaxation through dephasing,” *Phys. Rev. A* **103**, 022206 (2021).
- [50] Charlie R. Hogg, Federico Cerisola, James D. Cresser, Simon A. R. Horsley, and Janet Anders, “Enhanced entanglement in multi-bath spin-boson models,” *Quantum* **8**, 1357 (2024).
- [51] Luis A. Correa and Jonas Glatthard, “Potential renormalisation, lamb shift and mean-force gibbs state – to shift or not to shift?” *arXiv:2305.08941* (2023).
- [52] Keith H. Hughes, Clara D. Christ, and Irene Burghardt, “Effective-mode representation of non-Markovian dynamics: A hierarchical approximation of the spectral density. I. Application to single surface dynamics,” *J. Chem. Phys.* **131**, 024109 (2009).
- [53] Jake Iles-Smith, Arend G. Dijkstra, Neill Lambert, and Ahsan Nazir, “Energy transfer in structured and unstructured environments: Master equations beyond the Born-Markov approximations,” *J. Chem. Phys.* **144**, 044110 (2016).
- [54] Nicholas Anto-Sztrikacs and Dvira Segal, “Strong coupling effects in quantum thermal transport with the reaction coordinate method,” *New J. Phys.* **23**, 063036 (2021).
- [55] Luis A. Correa, Bujing Xu, Benjamin Morris, and Gerardo Adesso, “Pushing the limits of the reaction-coordinate mapping,” *J. Chem. Phys.* **151**, 094107 (2019).
- [56] Jake Iles-Smith, Neill Lambert, and Ahsan Nazir, “Environmental dynamics, correlations, and the emergence of noncanonical equilibrium states in open quantum systems,” *Phys. Rev. A* **90**, 032114 (2014).
- [57] The expression for Γ_{eff}^x appeared in Ref. [45] with a typing mistake there: Where Δ appeared, it should have been 2Δ for the qubit energy gap. This typo was corrected here.
- [58] Marlon Brenes, Brett Min, Nicholas Anto-Sztrikacs, Nir Bar-Gill, and Dvira Segal, “Bath-induced interactions and transient dynamics in open quantum systems at strong coupling: Effective hamiltonian approach,” *The Journal of Chemical Physics* **160**, 244106 (2024).
- [59] Larry Chen, Kan-Heng Lee, Chuan-Hong Liu, Brian Marinelli, Ravi K. Naik, Ziqi Kang, Noah Goss, Hyunseong Kim, David I. Santiago, and Irfan Siddiqi, “Scalable and site-specific frequency tuning of two-level system defects in superconducting qubit arrays,” (2025), *arXiv:2503.04702* [quant-ph].
- [60] Ted Thorbeck, Zhihao Xiao, Archana Kamal, and Luke C. G. Govia, “Readout-induced suppression and enhancement of superconducting qubit lifetimes,” *Phys. Rev. Lett.* **132**, 090602 (2024).
- [61] Anael Ben-Asher, Antonio I. Fernández-Domínguez, and Johannes Feist, “Memory loss is contagious in open quantum systems,” (2024), *arXiv:2402.16096* [quant-ph].
- [62] T. W. Ebbesen, “Hybrid light-matter states in a molecular and material science perspective,” *Accounts of Chemical Research* **49**, 2403–2412 (2016).
- [63] A. Thomas, L. Lethuillier-Karl, K. Nagarajan, R. M. A. Vergauwe, J. George, T. Chervy, A. Shalabney, E. Devaux, C. Genet, J. Moran, and T. W. Ebbesen, “Tilting a ground-state reactivity landscape by vibrational strong coupling,” *Science* **363**, 615–619 (2019).
- [64] Marlon Brenes, Jakub Garwoła, and Dvira Segal, “Optimal qubit-mediated quantum heat transfer via non-commuting operators and strong coupling effects,” (2025), *arXiv:2501.04220* [quant-ph].
- [65] Anqi Mu, Bijay Kumar Agarwalla, Gernot Schaller, and Dvira Segal, “Qubit absorption refrigerator at strong coupling,” *New Journal of Physics* **19**, 123034 (2017).
- [66] Hava Meira Friedman, Bijay Kumar Agarwalla, and Dvira Segal, “Quantum energy exchange and refrigeration: a full-counting statistics approach,” *New Journal of Physics* **20**, 083026 (2018).
- [67] A. Kato and Y. Tanimura, “Hierarchical equations of motion approach to quantum thermodynamics,” in *Thermodynamics in the Quantum Regime. Fundamental Theories of Physics*, Vol. 195, edited by F. Binder, L. A. Correa, C. Gogolin, J. Anders, and G. Adesso (Springer, 2018) pp. 579–595.
- [68] Gerald E. Fux, Piper Fowler-Wright, Joel Beckles, Eoin P. Butler, Paul R. Eastham, Dominic Gribben, Jonathan Keeling, Dainius Kilda, Peter Kirton, Ewen D. C. Lawrence, Brendon W. Lovett, Eoin O'Neill, Aidan Strathearn, and Roosmarijn de Wit, “Oqupy: A python package to efficiently simulate non-markovian open quantum systems with process tensors,” *The Journal of Chemical Physics* **161**, 124108 (2024).
- [69] Neill Lambert, Salim Ahmed, Mauro Cirio, and Franco Nori, “Modelling the ultra-strongly coupled spin-boson model with unphysical modes,” *Nature Communications* **10**, 3721 (2019).